UC Irvine
UC Irvine Electronic Theses and Dissertations

Title

Acoustic Radiation Force Elastic Microscopy for the Study of Corneal Elasticity

Permalink

Author

Mikula, Eric Robert

Publication Date

2015

UNIVERSITY OF CALIFORNIA,
IRVINE

Acoustic Radiation Force Elastic Microscopy for the Study of Corneal Elasticity

DISSERTATION

submitted in partial satisfaction of the requirements
for the degree of

DOCTOR OF PHILOSOPHY

in Biomedical Engineering.

by

Eric Robert Mikula

Dissertation Committee:
Professor Tibor Juhasz
Professor James Jester
Professor Donald Brown

2015

Dedicated to one Alisa Naret, who left us so soon.

TABLE OF CONTENTS

LIST OF FIGURES

ACKNOWLEDGEMENTS

I am truly grateful for the support I have received from so many people along the way through graduate studies at UCI. My family has been incredibly supportive and understanding. To my mother Luba, father Mario, and brother Mario Jr, this would have been a hard road without your guidance and unwavering devotion to telling me to hurry up and graduate already.

I thank my advisor, Tibor Juhasz, for his steadfast guidance and leadership. I thank Donald Brown and James Jester whose genuine enthusiasm for science has always been inspiring. I thank my committee as a whole, to all the meetings, to all the conferences, to all the work, to getting to know you all.

Finally, I'd like to thank those of my colleagues who I had the privilege of working with in the lab: Dongyul Chai, Moritz Winkler, Gautam Chaudhary, and the famous Hui Sun.

CURRICULUM VITAE

Eric Mikula

2006   B.S. in Biomedical Engineering, University of California, Irvine

2007   M.S. in Biomedical Engineering, University of California, Irvine

2015   Ph.D. in Biomedical Engineering, University of California, Irvine

FIELD OF STUDY

Corneal Biomechanics.

PUBLICATIONS

Mikula, E., Hollman, K., Chai, D., Jester, J. V., & Juhasz, T. (2014). Measurement of Corneal Elasticity with an Acoustic Radiation Force Elasticity Microscope. Ultrasound in medicine & biology, 40(7), 1671-1679.

Sun, H., Hosszufalusi, N., Mikula, E. R., & Juhasz, T. (2011). Simulation of the temperature increase in human cadaver retina during direct illumination by 150-kHz femtosecond laser pulses. Journal of biomedical optics, 16(10), 108001-108001.2011.

Sun, H., Kurtz, R. M., Mikula, E. R., & Juhasz, T. (2011). Temperature increase in porcine cadaver iris during direct illumination by femtosecond laser pulses.Journal of Cataract & Refractive Surgery, 37(2), 386-391. 2011.

Chai, D., Chaudhary, G., Mikula, E., Sun, H., Kurtz, R., & Juhasz, T. (2010). In vivo femtosecond laser subsurface scleral treatment in rabbit eyes. Lasers in surgery and medicine, 42(7), 647-651. 2010.

Sun, H., Mikula, E., Kurtz, R. M., & Juhasz, T. (2010). Temperature increase in human cadaver retina during direct illumination by femtosecond laser pulses.Journal of refractive surgery (Thorofare, NJ: 1995), 26(4), 272-277. 2010.

Chai, D., Chaudhary, G., Mikula, E., Sun, H., & Juhasz, T. (2008). 3D finite element model of aqueous outflow to predict the effect of femtosecond laser created partial thickness drainage channels. Lasers in surgery and medicine,40(3), 188-195. 2008.

ABSTRACT OF THE DISSERTATION

Acoustic Radiation Force Elastic Microscopy for the Study Corneal Elasticity

By

Eric Robert Mikula

Doctor of Philosophy in Biomedical Engineering

University of California, Irvine, 2015

Professor Tibor Juhasz Irvine, Chair

Abstract: The human cornea is a complex, inhomogeneous layered structure which acts as our window to the world. The mechanical properties of the cornea, along with the underlying corneal microstructure help determine the shape of the corneal surface, and thus also determine visual acuity. Since the cornea provides nearly two thirds of the refractive power of the eye, even small alteration of the corneal surface can have significant impact on the quality of vision. Furthermore, understanding corneal mechanics is useful when considering refractive disorders in the cornea such as keratoconus, while also providing a better understanding of the corneal response to refractive surgery or collagen cross linking procedures.

To investigate corneal elastic properties we developed an acoustic radiation force elasticity microscope (ARFEM). ARFEM applies a low frequency, high intensity acoustic radiation force to axially displace a femtosecond laser generated micro-bubble, while using a high frequency, low intensity ultrasound to monitor the position of the micro-bubble within the cornea. The maximum displacement of the micro-bubble is inversely proportional to elastic modulus. We found that the overall stiffness of the human cornea varies considerably throughout its volume. The anterior cornea is significantly stiffer than the posterior in the central and middle cornea, with the trend reverses at the periphery near the limbus. We also evaluated the effects of non-linear optical cross-linking and demonstrated the ability of the procedure to stiffen the cornea.

CHAPTER 1

INTRODUCTION

1.1 The Cornea and General Structure

The human eye consists of two elements which focus light onto the retina, namely, the cornea and the crystalline lens. The basic anatomy of the eye is shown in Figure 1.1. These two components provide the eye with an optical power of 60 diopters (D), with the cornea providing roughly 2/3 of the total power. The variable focus lens provides the remaining 20 D but can increase temporarily up to 33 D during accommodation. Thus the air-anterior cornea boundary is paramount to maintaining normal vision and even slight alterations on this surface can cause significant optical aberrations and reduce the quality of vision. The mechanical properties of the cornea are inextricably related to the physical corneal structure, much in the same way as the mechanics of a bridge are tied to the organization of the trusses and beams that compose it. Thus, a reliable measurement of biomechanical properties can shed light on the effects of the underlying corneal structure, and can serve as a diagnostic tool. Specifically, such measurements could aid in the early diagnosis of keratoconus (KC) as well as aid in screening patients before laser in situ keratomileusis (LASIK) to mitigate the risk of post LASIK ectasia. Keratoconus is a disorder characterized by a thinning of the cornea in addition to an outward protrusion of the cornea into a conical configuration. The resulting astigmatism and myopia have a dramatic negative effect on visual acuity, often necessitating a corneal transplant. While there is no consensus on the prevalence of keratoconus, estimates are in the range of 1 in 2000 [Rabinowitz 1998, Patel and Vellara 2015]. Likewise, post LASIK ectasia is marked by corneal thinning and

a progressive steepening of the curvature resulting in astigmatism, myopia, and reduced visual acuity. Estimates of the condition's prevalence range from 0.02% to 0.6% of LASIK patients [Tatar et al. 2014]. The surgical disruption of the corneal tissue is thought to exacerbate structural/biomechanical deficiencies that were undetected prior to LASIK. Early detection of compromised biomechanical properties is thus very useful for treatment purposes.

The cornea and sclera comprise the outer tunic of the eye, which is filled with vitreous and aqueous humor behind and in front of the lens, respectively. The intraocular pressure (IOP) is 15-18 mmHg and this stress is distributed throughout the structure of the sclera and cornea. The cornea is roughly 12 mm in diameter can be viewed as a tissue with 5 distinct layers: the epithelium, anterior limiting lamina (ALL or Bowman's membrane), stroma, posterior limiting lamina (Descemet's membrane), and the endothelium, as shown in Figure 2.2. While this layered view is convenient, it should be noted that that there is no distinct boundary between Bowman's and the anterior stroma. The central corneal thickness varies depending on the method of measurement, however a meta analysis of numerous studies employing varying methods revealed an average mean central corneal thickness (CCT) of 536 μm ± 31 μm [Doughty and Zaman 2000]. The stroma makes up roughly 90% of the corneal thickness and is composed of collagen lamellae spanning from limbus to limbus and parallel to the surface of the cornea. The limbus lies at the corneoscleral junction. At the central region of the cornea there are roughly 300 lamellae stacked at angles varying from 0 to 90° between one another. This increases to roughly 500 lamellae at the limbus. The lamellae are roughly 2 μm thick by up to 200 μm wide and are composed of parallel collagen fibrils that are roughly 31 nm in diameter [Meek and Boote 2003]. X-ray scattering imaging revealed two preferred orthogonal lamellae orientations in the inferior-superior and nasal-temporal directions. As these lamellae approach the limbus they adapt a

tangential orientation and merge with the circumferential fibril population of the limbal annulus [Boote and Meek 2009]. The tensile strength of the cornea, necessary to distribute the stress of IOP and maintain corneal shape, arises from the collagen fibers in the stroma and anterior limiting lamina (ALL). The organization of collagen determines the ability of the structure as a whole to distribute the load and resist strain or deformation [Vellara and Patel 2015]. The collagen scaffold, which accounts for 70% of the dry weight of the cornea, is set in an aqueous extrafibrillar matrix containing among other things proteoglycans, glycoproteins, and keratocytes.

An important difference exists structurally between the lamellae of anterior and posterior cornea. It has been shown that there is significant interweaving and bifurcation of stromal lamellae in the anterior cornea, with lamellae diverging from the parallel orientation and inserting upward in Bowman's membrane [Komai and Ushiki 1991, Radner et al. 1998, Radner et al. 2002, Jester et al. 2010]. Transmission electron microscopy revealed that collagen fibril bundles in the anterior stroma branched and inserted into the ALL at a density of 5.4 ± 0.8 insertions per 100 μm. Likewise, ALL originating fibril bundles appeared to insert into the anterior stroma at a rate of 29.8 bundles per 100 μm [Mathew et al. 2008]. In an effort to further quantify the interweaving of anterior stroma with the ALL, non linear optical high resolution macroscopy (NLO-HRMac) was used to measure lamellar branching point density (BPD). BPD was defined as a measure of collagen fiber connectivity. It was found that BPD decreased from 26.6/mm just beneath the ALL to 8.7/mm halfway through the stroma [Winkler et al. 2011]. These findings suggested that not only did collagen fibers from the anterior stroma insert in the the ALL, but that they actually intertwined with the ALL. Additionally, this study correlated BPD with elastic modulus at varies depths using needle indentation elastography. The higher

branched anterior region was found to be nearly twice as stiff as the mid and posterior regions. This finding was supported by earlier works which found that lamellar interweaving markedly increases interlamellar cohesive strength [Smolek and McCarey 1990, Smolek 1993] and protects the anterior region of the cornea against extreme swelling [Muller et al. 2001].

The structure of the cornea is highly inhomogeneous, varying both along the optical anterio-posterior axis as well as radially from the central to peripheral cornea. Lamellae tend to run parallel to the corneal surface posteriorly, while branching and interweaving in the anterior. Likewise, the in-plane horizontal orientation of lamellae changes from preferential orthogonal nasal-temporal/inferior-superior meridians centrally to circumferential/tangential directions at the limbus. As mentioned earlier, the biomechanical properties of the cornea are inherently linked to the structure of the cornea and it should come as no surprise that methods to quantify these mechanical properties have been the subject of much research throughout the years.

1.2 Methods to Measure Corneal Elasticity

The reported values of corneal elasticity in the literature span several orders of magnitude ranging from a few kilopascals to tens of megapascals [Winkler et al. 2011, Nyquist 1968, Hoeltzel 1992, Zeng 2001, Wang et al. 1996]. The reported values largely depend on the type of elastography methodology employed. Additionally, the type of elastic modulus varies in the reported values. Namely, the three most prominent are the tensile modulus, compressive modulus, and the shear modulus. Whereas a traditional tensile strip test will measure tissue strength along the direction of collagen fiber orientation, a compressive test will measure the resistance of the cornea to compression along the optical axis through its thickness. The shear modulus is a measure of the resistance of adjacent layers to 'sliding' past one another. In the

classic approach of strip testing a rectangular shaped sample is excised from the cornea and is then mechanically stretched with increasing force to calculate stress strain curves. Early strip testing determined the tensile elastic modulus of the human cornea to be roughly 4-14 MPa at a strain of 4% [Nyquist 1968, Hoeltzel 1992, Zeng 2001]. The reported values in the MPa regime make good sense since the primary type of collagen in the corneal stroma is type I collagen [Newsom et al. 1982]. Type I collagen is found in ligaments and tendons and is known for its mechanical strength. Recently uniaxial strip testing has been used to evaluate the effect of ultraviolet collagen cross-linking (CXL) on elasticity [Schumacher et al. 2011]. Strip testing was also used to correlate mechanical behavior of the cornea to stromal structure by subjecting corneal strips to uniaxial tension along different directions [Elsheikh and Alhasso 2009]. Strip testing lacks the ability to measure the spatial distribution of elastic properties without physically sectioning the cornea into strips from varying regions. Furthermore, addressing elasticity at different axial depths within the cornea to explore non-homogeneity along that axis is confounded by the need to physically excise the layer of interest. Other purely mechanical measurements of corneal elasticity utilized globe inflation methods and yielded values of 0.25 MPa to 17 MPa [Woo et al. 1972, Jue and Maurice 1986, Shin et al. 1997, Hjortdal 1995, Hjortdal 1996, Elsheikh et al. 2007]. Globe inflation assesses elasticity by measuring the displacements of external markers on the corneal surface in response to varying intraocular pressure (IOP). While globe inflation measures a bulk elastic modulus for the entire cornea, or potential elasticity variations across the corneal surface, it clearly lacks the capability to measure the depth dependence of corneal elasticity. Both strip extensiometry and globe inflation essentially measure the tensile strength of parallel collagen fibers without the ability to account for depth resolution.

Atomic force microscopy has been used to measure the depth dependence of the elastic modulus in the sectioned cornea [Last et al. 2012]. Reported values were in the tens of KPa. In a different study, the measurement of the transverse shear modulus at varying depths was described using torsional rheometry [Petsche et al. 2012]. Both of these methods involved physically sectioning the corneal sample to access the different layers and also had limitations in depth and lateral resolution. However, interesting differences in mechanical properties between the anterior and posterior cornea were observed. The Ocular Response Analyzer (ORA) (Reichert, Buffalo, New York) measures the deformation of the cornea in response to a brief puff of air and returns a metric called corneal hysteresis factor, which is presented as a measure of the viscous damping [Luce et al. 2004, Bayoumi et al. 2010]. The viscous damping factor is calculated from the pressure difference between the two moments where corneal applanation is achieved, corresponding to the inward and outward displacements of the cornea in response to the air puff. This phenomenon is related to corneal elasticity, viscous shear modulus, and the thickness of the cornea. Minus the thickness, these values cannot be calculated from the ORA measurement [Tanter et al. 2009]. The ORA is currently the only commercially available system capable of measuring corneal mechanical properties. Since this method does not require corneal sectioning it has gained limited use in clinical practice.

Various ultrasonic methods have also been developed for probing the elastic properties of tissues. These methods involve a mechanical perturbation of the tissue and subsequent ultrasound imaging of the resultant tissue displacement. Shear wave elasticity imaging uses a focused acoustic radiation force to generate shear waves within a tissue. The transverse strain generated by the shear waves is imaged and related to the shear elasticity of the tissue [Saryvazyan et al. 1998]. The force is generated through change in momentum of high intensity

acoustic waves as they are partially absorbed within the focal volume. The amount of force generated is related to the acoustic intensity and the tissue absorption coefficient. Using focused ultrasound to generate body force within a tissue has the distinct advantage of being capable of palpating localized volumes within a tissue that would otherwise be inaccessible. Supersonic shear imaging also uses focused acoustic radiation force to generate shear waves within a tissue, which are imaged and related to elasticity. The acoustic radiation force is sequentially focused at increasing depths within the sample at a rate that is faster than the speed of the shear wave (i.e supersonic), which typically has a velocity of just a few meters per second. The resultant shear waves constructively interfere and create high amplitude plane-shear waves along the Mach cone [Bercoff et al. 2004, Tanter et al. 2009]. The shear wave is imaged via tracking the strain induced speckle in tissue, with shear wave velocity being related to elasticity. Supersonic shear imaging has been used to evaluate the efficacy of photodynamic Riboflavin/UVA induced corneal CXL [Tanter et al. 2009]. Surface wave elastometry measures the speed of acoustic surface waves travelling parallel to the orientation of corneal collagen fibers and relates the propagation velocity to elasticity [Dupps et al. 2007]. Similarly, OCT has been used to measured shear wave speed in the cornea in response to mechanical perturbation of the corneal surface by a wire [Manapuram et al. 2012]. A variation of this method used an acoustic radiation force to perturb the tissue while using OCT to image the tissue vibration [Qi et al. 2012, Wang 2012]. Acoustic radiation force impulse (ARFI) imaging uses high intensity, focused ultrasound pulses to directly induce a displacement in the tissue. The displacement of the tissue is tracked using pulse-echoes and is related to the mechanical properties of the tissue [Nightingale et al. 2003]. A similar method images corneal strain induced by a metal plate using an ultrasound elasticity microscope [Hollman 2002 et al., Hollman et al. 2013]. The ultrasound elasticity imaging techniques

described above rely on speckle tracking methods to create the strain images. Elastic properties are calculated from the complex displacement field. Difficulties with these techniques arise from the cornea being a weak absorber of ultrasound. This results in small tissues displacements which must then be imaged via acoustic speckle tracking. Furthermore, the cornea is relatively anechoic and has limited ultrasonic speckle, further compounding the problem of imaging minute tissue strain.

Brillouin microscopy has seen renewed interest in recent years due in part to non conventional spectrometers with increased imaging speed and sensitivity in the GHz range [So 2008]. Brillouin scattering is an inelastic process where light interacts with thermally induced density fluctuations, also known as acoustic phonons [Vaughan and Randall 1980, Scarcelli et al. 2012]. The phonons induce a frequency shift in the scattered light on the order of a few GHz. The frequency shift is related to the Brillouin elastic modulus of the material, which is typically measured in the gigapascal range for the cornea.

1.3 Acoustic Radiation Force Elastic Microscopy

Acoustic radiation force elastic microscopy (ARFEM) uses a low frequency, high intensity acoustic force to displace a femtosecond laser generated microbubble, while using a high frequency, low intensity ultrasound to monitor the position of the microbubble within the tissue [Erpelding et al. 2005]. The method was used to measure age related elasticity changes in the human lens [Erpelding et al. 2005]. Likewise, this method was used to probe the elastic properties of tissue mimicking gelatin phantoms and showed good agreement with direct uniaxial compression testing [Yoon et al. 2011]. The elastic modulus is related to the displacement of the microbubble within the tissue rather than tissue strain. Unlike other ultrasonic elasticity methods,

ARFEM does not rely on the absorption of acoustic energy to induce tissue strains large enough to image. Rather, acoustic radiation is used to perturb a temporary contrast agent in the form a micro bubble. This is especially useful since the cornea is relatively anechoic and a weak absorber of acoustic energy. The acoustic impedance mismatch between the cornea and gas bubble is large enough to make the bubble a perfect reflector of acoustic energy within the cornea. Compared with a perfect absorber, a perfect reflector experiences two times the body force as the acoustic waves are not only stopped, but reversed as well. ARFEM has the advantage of improved depth resolution over other ultrasonic methods as the elasticity measurement is localized to the exact position of a microscopic bubble. The local elasticity is simply related to bubble displacement as opposed to a complex strain image. The location of the elasticity measurement depends solely on the location of the bubble, which can be created anywhere without the need to section the cornea. This is in part due to the high transmission of visible and near infrared light in the cornea, which is well above 90% at 800 nm (van den Berg and Spekreijse 1997).

The focus of this work is the adaptation of the ARFEM technique to measure spatial distribution of elasticity in the human cornea. A 3D elasticity map of the cornea can be created and compared with local collagen lamellae structure. Since interweaving collagen fibers are especially abundant in the anterior regions of the cornea and their density markedly decreases in the posterior region, the measurement of localized corneal elasticity as a function of depth across the entire thickness of the tissue is important. ARFEM was chosen since it can provide data on the depth dependence of the corneal elasticity obtained without having to dissect the cornea to access various layers.

1.4 Laser Induced Optical Breakdown (LIOB)

The bubbles used for ultrasonic measurement in this research are generated through laser induced optical breakdown (LIOB). During this process, the cornea non-linearly absorbs photons resulting in free electron generation via multiphoton ionization and/or avalanche ionization. Once the threshold free electron density has been achieved, LIOB occurs. Ionization as it pertains to LIOB occurs when an atom or molecule loses electrons. During multiphoton ionization (MPI), multiple photons are directly absorbed by a valence electron. Once the band gap energy is exceeded the electron is excited to the quasi-free conduction band. Depending on the pulse duration, this process can either dominate or produce seed electrons for further ionization. Avalanche ionization occurs when a free electron absorbs photons through inverse bremsstrahlung absorption, thus gaining kinetic energy and freeing other bound electrons through impact ionization. These free electrons subsequently absorb photons and accelerate, freeing other electrons establishing the avalanche process. The dominant process depends on the pulse length of energy used, with a transition happening in the femtosecond regime (10^{-15} seconds). For pulse durations greater than 100 fs avalanche ionization is the dominant process, while multiphoton processes are negligible [Loesel et al. 1996]. For pulse durations less than 100 fs there is a transition from avalanche to multiphoton processes as the time lag between collisions that result in inverse bremsstrahlung absorption becomes relevant [Bloembergen 1974, Hammer et al. 1996]. LIOB occurs when the free electron density exceeds 10^{18}-10^{21}/cm^3, with gases and condensed matter at the lower and upper limits, respectively [Barnes and Rieckhoff (1968), Yablonovitch and Bloembergen 1972, Vogel et al. 1990, Vogel and Venugopalan 2003]. With a fs laser, the initial high temperature causes the plasma volume to quickly expand, causing an acoustic shockwave in the surrounding tissue, which dissipates within 20 ns and corresponds

to a radius of 20µm [Juhasz et al. 1997]. The free electrons and ions then recombine as gas creating the cavitation bubble. The entire process is known as photodisruption.

Femtosecond laser pulses have several distinct advantages over longer pulses. The threshold fluence for LIOB is dramatically reduced with decreasing pulse duration. For the human cornea, the threshold fluence for 200 ps pulses is 40 J/cm^2, the threshold fluence for 350 fs pulses is only 2 J/cm^2 [Loesel et al. 1996]. Femtosecond laser photodisruption is known to cause an ultra small damage zone and minimal collateral damage to surrounding tissue [Schaffer 2002, Glezer 1998]. Damage zones as small as 10nm in solids and 200nm in biological material have been observed [Joglekar 2005, Maxwell 2005, Lubatchowski 2002]. The mechanical shockwave associated with LIOB is also mitigated with shorter pulses. Estimates indicate that the volume of tissue affected by the induced shockwave is 1000 times less for a femtosecond breakdown when compared with picoseconds breakdown. Furthermore, cavitation bubble radius and lifetime are also dramatically reduces with the use of femtosecond pulses [Juhasz et al. 1997]. The size of the cavitation bubbles can be controlled by varying the F-number of the focusing lens, the beam intensity, and the number of pulses delivered to the tissue [Kennedy 1995, Loesel 1996, Juhasz 1997].

For these reasons the femtosecond laser has seen widespread clinical use in ophthalmology. The femtosecond laser was proposed for flap cutting in the LASIK procedure and has since been commercialized and been used in an estimated 30-50% of all LASIK procedures (Juhasz et al. 1999, Salomao et al. 2010]. Similarly, the femtosecond laser has seen increasing use in cataract surgery, lens capsulotomy, and lens fragmentaion [Hodge et al. 2012, Trikha 2015]. The femtosecond laser has also been investigated in the treatment of glaucoma with respect to pressure reduction in the eye [Chai et al. 2010]. The ability to precisely control

the location and size of the cavitation bubble in addition to low collateral damage make the femtosecond laser ideal for this research.

1.5 Hypothesis and Specific Aims

The focus this research is to combine a femtosecond laser with an acoustic radiation/imaging ultrasound to probe the elastic properties of the human cornea. The hypothesis is that application of acoustic radiation force to a femtosecond laser generated bubble and subsequent imaging of the bubble displacement can allow spatially resolved measurement of corneal elastic properties. First, a femtosecond laser is used to reliably create a bubble at a desired location within the cornea via LIOB. Then, a custom confocal ultrasound transducer focused on the bubble applies a calibrated acoustic radiation force to displace the bubble as low intensity imaging pulse-echoes simultaneously track the position of the bubble. The raw RF data is processed offline to reveal the displacement of the bubble, which is used to calculate local elasticity. The goal of this research is to construct and test an acoustic radiation force elasticity microscope, and to measure the elastic properties of the human cornea.

This research can provide new insights into the mechanical environment within the cornea and its relation to structure. In addition to adding to the general scientific knowledge base concerning the cornea, these results can have implications in the understanding of mechanically/structurally compromised corneas as in the case of keratoconus, as well as the potential to serve as a preoperative screen for patients susceptible to post LASIK ectasia. The minimization of collateral damage inherent to the use of femtosecond pulses is also promising with respect to the extension of the methodology to in vivo application.

To achieve the aims, an acoustic radiation force elasticity microscope must be first designed, tested, and optimized. Subsequently, cornea elasticity measurements can be achieved. To achieve this the following specific aims were undertaken.

1.5.1 Aim I – ARFEM System

Build an ARFEM system. A confocal transducer capable of generating sufficient force while simultaneously imaging at an adequate resolution is necessary. An optical-acoustic set-up needs to be devised to allow synchronized bubble generation and acoustic measurement/force generation.

1.5.2 Aim II – Ultrasound Characterization

Both the inner and outer piezoelectric elements of the confocal transducer (imaging and force generating elements, respectively) need to be characterized. Both beam profile and intensity should be measured.

1.5.3 Aim III – Validation in Tissue Phantom/Porcine Cornea

Confirm that the technique is capable of measuring bubble displacement in tissue mimicking phantoms of known mechanical properties.   Also, confirm that measurements are possible within the porcine cornea.

1.5.4 Aim IV – Optimization of ARFEM technique

Eliminate effects of standing waves. Optimize force pulse waveform to reduce noise in the RF signal.

1.5.5 Aim V - ex-vivo Human Cornea

1.5.5a Anterior vs. Posterior Cornea

Measure the difference in elasticity between the anterior and posterior cornea in the direction orthogonal to the cornea surface.

1.5.5b Cross Sectional Mapping

Measure the elastic properties across the entire cornea at varying depths by moving the corneal sample over the focal region with 3-D microstage.

1.5.6 Aim VI – Keratoconus and Crosslinked Corneas

Evaluate corneas with keratoconus. Evaluate the efficacy of corneal crosslinking using ARFEM.

1.6 Dissertation Overview

Chapter 2 introduces the mathematical theory and principles of acoustic radiation force elastic microscopy (ARFEM). A protocol is established for the creation of tissue mimicking gelatin phantoms and preliminary ARFEM measurements are made in gelatin. These results are compared with traditional compression measurements. Pilot measurements are made in porcine corneas. Chapter 3 describes the optimization process necessary to make reliable measurement in the human cornea. Standing waves in the acoustic chamber are continual source of error and are addressed by altering the laser objective focal length as well as the acoustic force radiation waveform. Furthermore, noise in the A-scan RF signal is reduced via a notched force pulse whereby imaging pulses are "hidden" within deliberately placed notches in the force pulse. Chapter 4 presents the results of measuring the elasticity of the cornea both axially and radially

across the cornea. Interesting results are found between the anterior and posterior cornea, both centrally and peripherally. Chapter 5 presents the result obtained from keratoconus corneas. Furthemore, preliminary measurements in crosslinked corneas are presented. Chapter 6 presents the conclusion and implication of this body of work. Further works are suggested and potential for clinical application is explored.
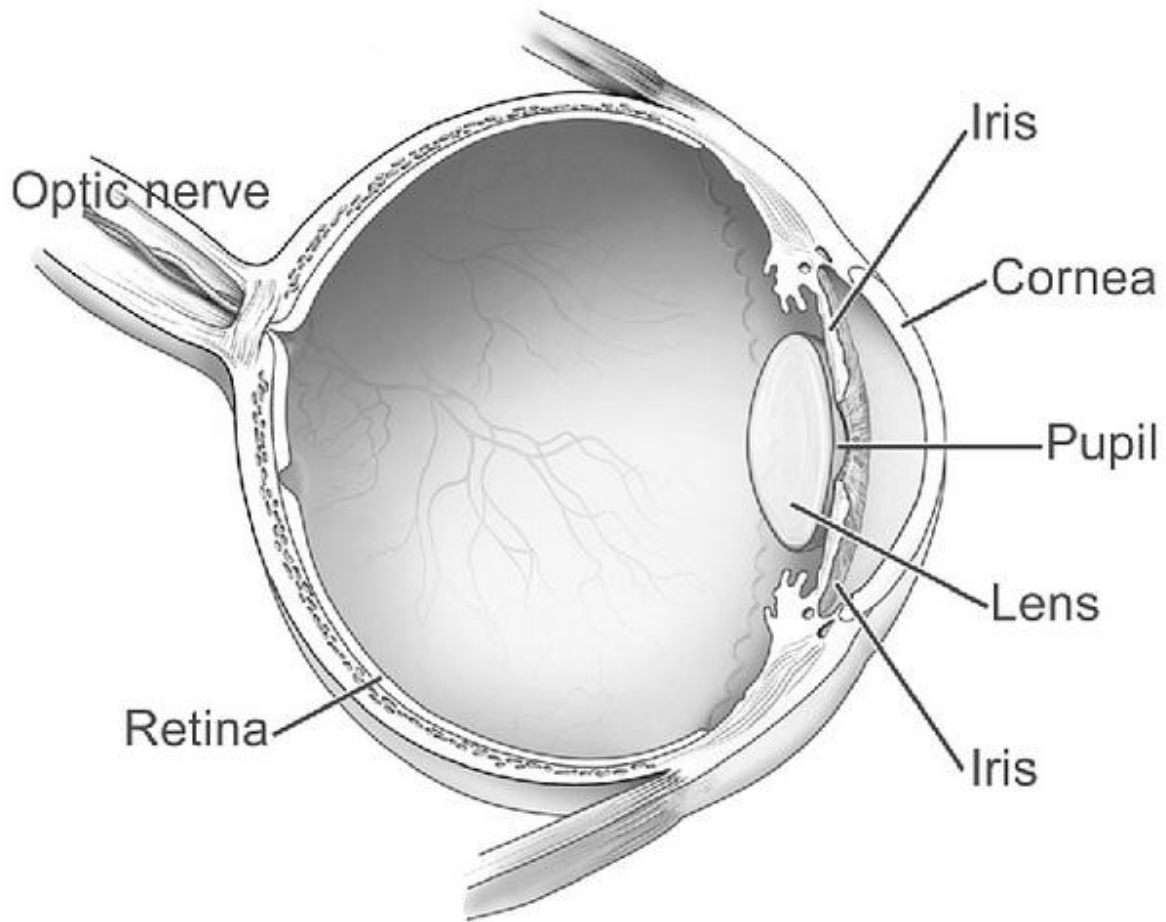
Figure 1.1 – Basic anatomy of the human eye. (source: National Eye Institute, the National Institutes of Health)
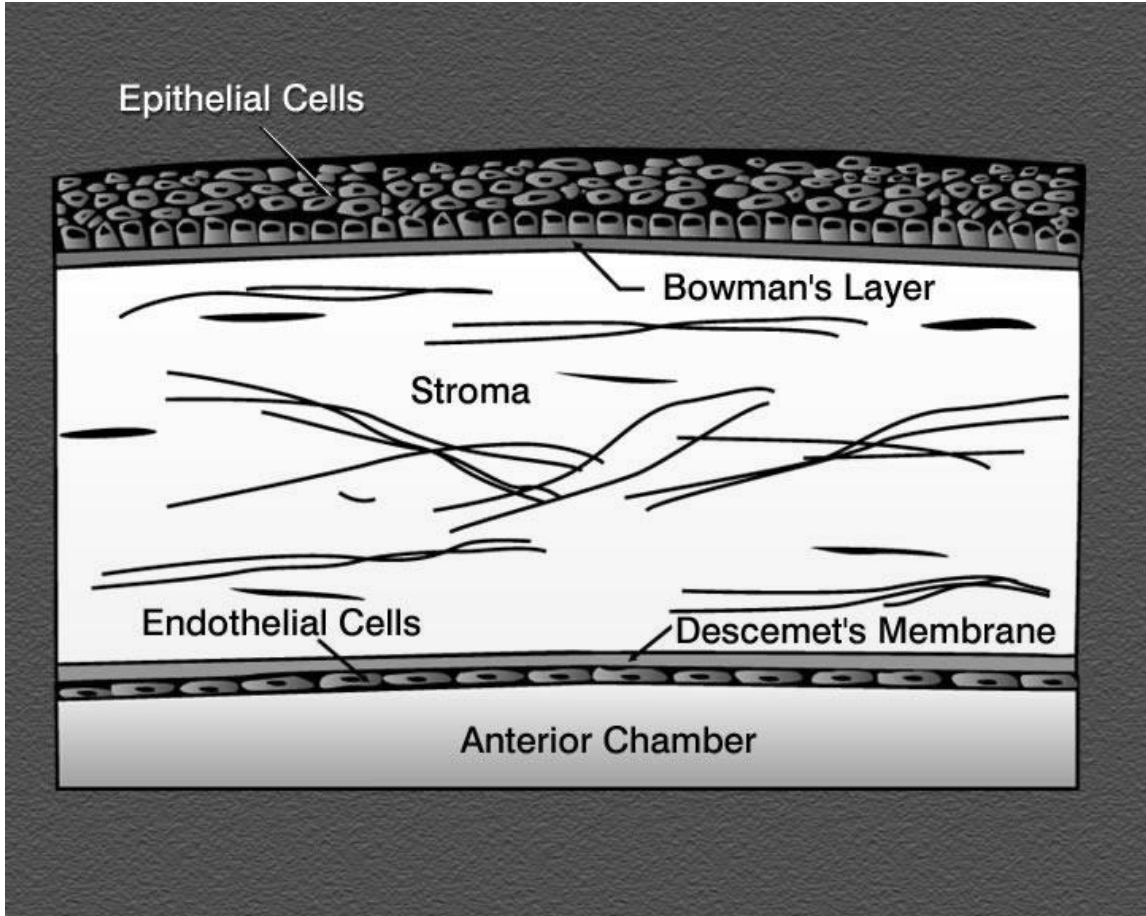
Figure 1.2 – The five layers of the human cornea.

1.7 References

Barnes, P.A., and Rieckhoff, K.E. "Laser induced underwater sparks." Appl. Phys. Lett. 13, 282-284. 1968.

Bayoumi NH, Bessa AS, El Massry AA. "Ocular response analyzer and goldmann applanation tonometry: a comparative study of findings." J Glaucoma. 19(9):627-31. 2010.

Bercoff, J.; Tanter, M.; Fink, M. "Supersonic shear imaging: a new technique for soft tissue elasticity mapping," Ultrasonics, Ferroelectrics and Frequency Control, IEEE Transactions on , vol.51, no.4, pp.396-409, April 2004.

Bloembergen N. "Role of cracks, pores, and absorbing inclusions on laser induced damage threshold at surfaces of transparent dielectrics." Appl Opt. 1973 Apr 1;12(4):661-4. 1973.

Boote C, Dennis S, Newton RH, Puri H, Meek KM. "Collagen fibrils appear more closely packed in the prepupillary cornea: optical and biomechanical implications." Invest Ophthalmol Vis Sci. 44(7):2941-8. 2003.

Chai, Dongyul et al. "In vivo femtosecond subsurface sclera treatment in rabbit eyes." Lasers in surgery and medicine42.7 (2010): 647–651. PMC. Web. 9 Feb. 2015.

Doughty MJ, Zaman ML. "Human corneal thickness and its impact on intraocular pressure measures: a review and meta-analysis approach." Surv Ophthalmol. 44(5):367-4   08. 2000.

Dupps WJ. Biomechanical modeling of corneal ectasia. J. Refr. Surg. 2005. 21:186-190. 2005.

Dupps WJ Jr, Netto MV, Herekar S, Krueger RR. "Surface wave elastometry of the cornea in porcine and human donor eyes." J Refract Surg. (1):66-75. 2007.

Eli Yablonovitch and N. Bloembergen. "Avalanche Ionization and the Limiting Diameter of Filaments Induced by Light Pulses in Transparent Media." Phys. Rev. Lett. 29, 907 − Published 2 October 1972.

Elsheikh A, Alhasso D. "Mechanical anisotropy of porcine cornea and correlation with stromal microstructure." Exp Eye Res. 88(6):1084-91. 2009.

Elsheikh A, Ross S, Alhasso D, Rama P. "Numerical study of the effect of corneal layered structure on ocular biomechanics." Curr Eye Res. 34(1):26-35. 2009.

Elsheikh A, Wang D, Pye D. "Determination of the modulus of elasticity of the human cornea." J Refract Surg. 23(8):808-18. 2007.

Erpelding T, Hollman K, O'Donnel M. "Bubble-based acoustic radiation force elasticity imaging." IEEE Trans Ultrason Ferroelectr Freq Control. 52:971-979. 2005.

Gerald W. Nyquist, Rheology of the cornea: Experimental techniques and results, Experimental Eye Research, Volume 7, Issue 2, April 1968, Pages 183-188.

Glezer EN, Schaffer CB, Nishimura N, Mazur E. "Minimally disruptive laser induced breakdown in water." Opt. Letter 1997. 22(23):1817-1819. 1997.

Hammer DX, Thomas RJ, Frenz M, Jansen ED, Noojin GD, Diggs SJ, Noack J, Vogel A, Rockwell BA. "Shock wave and cavitation bubble measurements of ultrashort pulse laser-induced breakdown in water." Proc SPIE-Int Soc Opt Eng 1996; 2681:437-448. 1996.

Hjortdal J O. Extensibility of the normo-hydrated human cornea. Acta ophthalmologica Scandinavica. 73. 12-17, 1995.

Hjortdal J O. Regional elastic performance of the human cornea. J. Biomechanics. 29:931-942. 1996

Hodge, Chris et al. "Femtosecond Cataract Surgery: "A Review of Current Literature and the Experience from an Initial Installation." Saudi Journal of Ophthalmology 26.1 (2012): 73–78. PMC. Web. 9 Feb. 2015.

Hoeltzel DA, Buzard K, Altman P. Experimental determination and comparison of the mechanical response of bovine and rabbit corneas as a model for predicting the mechanical behavior of the human cornea. J. Biomech. Eng. 1992, 114:202-215.

Hollman K, Emelianov S, Neiss JH, Jotyan G, Spooner G, Juhasz T, Kurtz R, O'Donnel M. Strain imaging of corneal tissue with an ultrasound elasticity microscope. Cornea 2002. 21:68-73. 2002.

Hollman KW, Shtein RM, Tripathy S, Kim K. "Using an ultrasound elasticity microscope to map three-dimensional strain in a porcine cornea." Ultrasound Med Biol. 2013 Aug;39(8):1451-9. 2013.

Jester JV1, Winkler M, Jester BE, Nien C, Chai D, Brown DJ. "Evaluating corneal collagen organization using high-resolution nonlinear optical macroscopy." Eye Contact Lens. 36(5):260-4. 2010.

Joglekar AP, H. Liu, G.J. Spooner, E. Meyhöfer, G. Mourou and A.J. Hunt. "A study of the deterministic character of optical damage by femtosecond laser pulses and applications to nanomachining." Applied Physics B: Lasers and Optics. Volume 77, Number 1, 25-30. 2005.

Jue B, Maurice D. The mechanical properties of the rabbit and human cornea, Journal of Biomechanics, Volume 19, Issue 10. Pages 847-853. 1986.

Juhasz T, Kastis G, Suarez C, Bor Z, Bron W. Time resolved observation of shock waves and cavitation bubbles generated by femtosecond laser pulses. Lasers IN Surgery and Medicine. 1997. 19:23-31. 1997.

Juhasz T, Loesel FH, Kurtz RM, Horvath C, Bille JF, Mourou G. "Corneal refractive surgery with femtosecond lasers." IEEE J Sel Top Quantum Electron 1999; 5(4):902 – 910. 1999.

Kennedy PA, Boppart SA, Hammer DX, Rockwell BA, Noojin GD, Roach WP. "A firstorder model for computation of laser-induced breakdown thresholds in ocular and aqueous media: part II comparison to experiment." IEEE J Quantum Electron 1995b; 31(12):2250-2257. 1995.

Kennedy PA. "A first-order model for computation of laser-induced breakdown thresholds in ocular and aqueous media: part I theory." IEEE J Quantum Electron 1995a; 31(12):2241-2249. 1995.

Loesel FH, Niemz MH, Bille JF, Juhasz T. "Laser-induced optical breakdown on hard and soft tissues and its dependence on the pulse duration: experiment and model." IEEE J Quantum Electron 1996; 32(10):1717-1722. 1996.

Lubatschowski H, Alexander Heisterkamp, Fabian Will, Ajoy I. Singh, Jesper Serbin, Andreas Ostendorf, Omid Kermani, Ralf Heermann, Herbert Welling, and Wolfgang Ertmer. "Ultrafast lasers for medical applications." Proc. of SPIE 2002. 4633:38-49. 2002.

Luce, David A. "Determining in vivo biomechanical properties of the cornea with an ocular response analyzer." Journal of Cataract & Refractive Surgery , Volume 31 , Issue 1 , 156 – 162. 2004

Manapuram RK, Aglyamov SR, Monediado FM, Mashiatulla M, Li J, Emelianov SY, Larin KV. "In vivo estimation of elastic wave parameters using phase-stabilized swept source optical coherence elastography." J Biomed Opt. 17(10):100501. 2012.

Mathew JH1, Bergmanson JP, Doughty MJ. "Fine structure of the interface between the anterior limiting lamina and the anterior stromal fibrils of the human cornea." Invest Ophthalmol Vis Sci. 49(9):3914-8. 2008.

Maxwell I, Samuel Chung, Eric Mazur. "Nanoprocessing of subcellular targets using femtosecond laser pulses." Medical Laser Application, Volume 20, Issue 3, 14 October 2005, Pages 193-200. 2005.

Meek KM, Boote C. "The use of X-ray scattering techniques to quantify the orientation and distribution of collagen in the corneal stroma." Prog Retin Eye Res. 28(5):369-92. 2009.

M K Smolek, B E McCarey .Interlamellar adhesive strength in human eyebank corneas. IOVS June 1990 31:1087-1095.

Muller L, Elisabeth Pels, Gijs F J M Vrensen. The specific architecture of the anterior stroma accounts for maintenance of corneal curvature. Br J Ophthalmol 2001;85:437-443

Newsome DA, Gross J, Hassell JR. "Human corneal stroma contains three distinct collagens." Invest Ophthalmol Vis Sci. 22(3):376-81. 1982.

Nightingale, K.; Palmeri, M.; Bouchard, R.; Trahey, G.; , "Acoustic radiation force impulse imaging: a parametric analysis of factors affecting image quality," Ultrasonics, 2003   IEEE Symposium on , vol.1, no., pp. 548- 553 Vol.1, 5-8 Oct. 2003.

Petsche SJ, Chernyak D, Martiz J, Levenston ME, Pinsky PM. "Depth-dependent transverse shear properties of the human corneal stroma." Invest Ophthalmol Vis Sci. 2012 Feb 21;53(2):873-80. 2012.

Rabinowitz YS. "Keratoconus." Survey Ophthalmology. 42(4):297-319. 1998.

Radner W, Mallinger R. Interlacing of collagen lamellae in the midstroma of the human cornea. Cornea. 2002. 21:6:598-601.

Radner W, Zehetmayer M, Aufreiter R, Mallinger R. Interlacing and cross-angle distribution of collagen lamellae in the human cornea. Cornea. 1998. 17:5:537-543.

S. L-Y Woo, A. S. Kobayashi, W. A. Schlegel, C. Lawrence, Nonlinear material properties of intact cornea and sclera, Experimental Eye Research, Volume 14, Issue 1, July 1972,   pg. 29-39

Salomão, Marcella Q., and Steven E. Wilson. "Femtosecond Laser in Laser in Situ Keratomileusis." Journal of cataract and refractive surgery 36.6 (2010): 1024–   1032. PMC. Web. 9 Feb. 2015.

Sarvazyan AP, Rudenko OV, Swanson SD, Fowlkes JB, Emelianov SY. "Shear wave elasticity imaging: a new ultrasonic technology of medical diagnostics." Ultrasound Med Biol. 24(9):1419-35. 1998.

Scarcelli, G. & Yun, S. H. "Brillouin Optical Microscopy for Corneal Biomechanics." Investigative Ophthalmology & Visual Science. Vol. 53, No. 1. 185-191. 2012.

Schaffer C, Nishimura N, Glezer E, Kim A, Mazur E. "Dynamics of femtosecond laser-induced breakdown in water from femtoseconds to microseconds." Opt Express. 2002 Feb 11;10(3):196-203. 2002.

Schumacher S, Oeftiger L, Mrochen M. "Equivalence of biomechanical changes induced by rapid and standard corneal cross-linking, using riboflavin and ultraviolet radiation." Invest Ophthalmol Vis Sci. 25;52(12):9048-52. 2011.

Shin T, Vito R, Johnson L, Bernard E. McCarey. The distribution of strain in the human cornea. Journal of biomechanics . volume 30 issue 5 Pages 497-503. 1997.

Smolek MK. Interlamellar cohesive strength in the vertical meridian of human eye bank corneas. IOVS September 1993 34:2962-2969.

Peter So. "Microscopy: Brillouin bioimaging." Nature Photonics 2, 13 - 14 (2008)

Tanter M, Touboul D, Gennisson JL, Bercoff J, Fink M. "High-resolution quantitative imaging of cornea elasticity using supersonic shear imaging." IEEE Trans Med Imaging. 2009 Dec;28(12):1881-93. 2009.

Tatar MG, Aylin Kantarci F, Yildirim A, Uslu H, Colak HN, Goker H, Gurler B. "Risk Factors in Post-LASIK Corneal Ectasia." J Ophthalmol. 2014. Epub 2014 Jun 3.

Trikha, S et al. "The Journey to Femtosecond Laser-Assisted Cataract Surgery: New Beginnings or a False Dawn?" Eye 27.4 (2013): 461–473. PMC. Web. 9 Feb. 2015.

Vaughan JM, Randall JT. "Brillouin scattering, density and elastic properties of the lens and cornea of the eye." Nature. Volume 284. 3:489-91. 1980.

Vellara HR1, Patel DV. "Biomechanical properties of the keratoconic cornea: a review." Clin Exp Optom. Jan;98(1):31-8. 2015 doi: 10.1111/cxo.12211.

Vogel, A.; Schweiger, P.; Frieser, A.; Asiyo, M.N.; Birngruber, R. "Intraocular Nd:YAG laser surgery: laser-tissue interaction, damage range, and reduction of collateral effects," Quantum Electronics, IEEE Journal of , vol.26, no.12, pp.2240-2260, Dec 1990.

Vogel A, Venugopalan V. "Mechanisms of pulsed laser ablation of biological tissues." Chem Rev. 2003 Feb;103(2):577-644. 2003.

Wang H, Prendiville PL, McDonnell PJ, Chang WV. "An ultrasonic technique for the measurement of the elastic moduli of human cornea." J Biomech. 29(12):1633-6. 1996.

Wang S, Li J, Manapuram RK, Menodiado FM, Ingram DR, Twa MD, Lazar AJ, Lev DC, Pollock RE, Larin KV. "Noncontact measurement of elasticity for the detection of soft- tissue tumors using phase-sensitive optical coherence tomography combined with a focused air-puff system." Opt Lett. 37(24):5184-6. 2012.

Winkler M1, Chai D, Kriling S, Nien CJ, Brown DJ, Jester B, Juhasz T, Jester JV. "Nonlinear optical macroscopic assessment of 3-D corneal collagen organization and axial biomechanics." Invest Ophthalmol Vis Sci. 11;52(12):8818-27. 2011.

Y Komai, T Ushiki. The three-dimensional organization of collagen fibrils in the human cornea and sclera. IOVS July 1991 32:2244-2258.

Yoon S, Aglyamov SR, Karpiouk AB, Kim S, Emelianov SY. "Estimation of mechanical properties of a viscoelastic medium using a laser-induced microbubble interrogated by an acoustic radiation force." J Acoust Soc Am. 130(4):2241-8. 2011.

Zeng Y, Yang J, Huang K. A comparison of biomechanical properties between human and porcine cornea. J Biomech. 2001, 34:533-537.

CHAPTER 2

ARFEM THEORY AND VALIDATION

2.1 Introduction

Elasticity measurements in the simplest terms are analogous to the well known Hooke's law:

$$F = kx. \qquad \text{eq. 2.1.1}$$

Hooke's law states the amount of force (F) required to distend or compress a spring by a given distance (x) is proportional to that distance. The constant of proportionality (k) is the stiffness of the spring, or spring constant. While this relation is applicable specifically to a linearly elastic spring, the underlying idea is the same for other elasticity measurements. Some known force is imparted on the material of interest (i.e. the cornea) and the response of the material is observed. Generally, the goal is to quantify the relationship between stress and strain in a material, otherwise known as the constitutive relation in a structural analysis. Stress (σ) in the simplest case is a force (F) applied to a material over the crossectional area (A) or

$$\sigma = F/A. \qquad \text{eq. 2.1.2}$$

Strain (ε) is a measure of the deformation of the material in response to the stress and is given by

$$\varepsilon = \Delta L/L. \qquad \text{eq. 2.1.3}$$

The elastic modulus (E) is defined as the ratio between stress and strain. Strip testing, for example, is a straightforward application of the generalization above [Nyquist 1968, Hoeltzel 1992, Zeng 2001, Elsheikh and Alhasso 2009]. A rectangular corneal strip of known dimension is put under tensile stress while the amount of stretch (strain) is measured. The elastic modulus is then directly calculated by dividing the stress by the strain. Globe inflation elasticity

measurements add a level of complexity by keeping the globe intact. The tensile stress is applied by varying the IOP, while the strain is measured somewhat indirectly via surface marker displacements [Woo et al. 1972, Jue and Maurice 1986, Shin et al. 1997, Hjortdal 1995, Hjortdal 1996, Elsheikh et al. 2007].

Following this reasoning, numerous ultrasonic techniques have been used to evaluate corneal tissue response to an acoustic radiation force. A distinct advantage of using an acoustic radiation force to induce strain is the ability to remotely palpate at any arbitrary location within the tissue. Methods utilizing acoustic radiation force include shear wave elasticity imaging, supersonic shear imaging, and acoustic radiation force impulse imaging [Saryvazyan et al. 1998, Bercoff et al. 2004, Tanter et al. 2009, Qi et al. 2012, Wang 2012, Nightingale et al. 2013]. These methods use tightly focused high intensity ultrasound to generate an acoustic radiation force within the tissue. Since the cornea fundamentally lacks endogenous reflectors of acoustic energy, these methods rely on the absorption of acoustic energy to generate a body force within the tissue. A body force acts throughout the volume of a body, which in this case is determined by the focusing geometry of the high intensity transducer. If an acoustic wave is partially absorbed there is necessarily a change in momentum of the propagating wave. By Newton's second law a change in momentum results in a body force acting on the absorbing volume within the medium given by

$$F = dp/dt, \qquad\qquad \text{eq. 2.1.4}$$

where 'F' is force and 'p' is momentum. The body force generates small displacements within the tissue which are tracked by low intensity ultrasound imaging pulse, or in some cases optical coherence tomography (OCT). Speckle tracking algorithms are typically used to render images of the tissue displacement within the absorbing volume as well as in the immediate vicinity. This

information is used to calculate the elastic properties of the interrogated volume. However, calculation of local elasticity is hindered by the complex strain field as well as the irregular shape of the interrogated region occupying the focal volume of the transducer.

Acoustic radiation force elastic microscopy (ARFEM) circumvents the problem of complex strain fields and irregular interrogation volumes by introducing an exogenous acoustic reflector to the cornea in the form of a femtosecond laser generated microbubble [Erpelding et al. 2005, Mikula et al 2014]. Since the method relies on reflection of acoustic energy, the force generated is not a body force but rather a normal point force, simplifying calculations. Furthermore, reflection is a far more effective avenue for generating acoustic radiation force when compared to attenuation. LIOB and the creation of bubbles in the cornea using femtosecond laser pulses are well established thus making ARFEM an ideal candidate for this research [Kennedy 1995, Loesel 1996, Juhasz 1997, Schaffer 2002, Glezer 1998].

This chapter will examine in greater depth the specific theory behind ARFEM, with attention paid to the generation of the acoustic radiation force and it's interaction with a gaseous bubble with the cornea. The method is then validated in gelatin phantoms of known mechanical properties. Measurements are made in the porcine cornea.

2.2 ARFEM Theory

During an ARFEM measurement a force is imparted on a micro-bubble embedded within an elastic medium, resulting in a displacement of the bubble. The acoustic force is turned off after which the bubble returns to its original position. Meanwhile, a low intensity imaging ultrasound tracks the displacement of the bubble. The generation of an acoustic force needs to be

considered, as well the bubble/medium response to the force. First we will consider the acoustic radiation force.

Ultrasound waves are pressure waves and carry momentum. In an elastic medium, a wave is either absorbed, reflected, or transmitted. For example, in a perfectly absorbing medium, the acoustic wave is totally absorbed resulting in a change in momentum from a finite amount to zero. By Newton's second law, a change in momentum results in a force. In this case it is the acoustic radiation force. A more efficient way of generating acoustic radiation force is through reflection, as the wave is first stopped and then reversed. Thus, perfect reflection generates twice the force of perfect absorption. The cornea is not an efficient absorber, nor does it possess significant inhomogeneities to reflect/scatter acoustic energy. However, the boundary between an aqueous medium such as the cornea and a gaseous bubble is nearly a perfect reflector, as given by

$$R = \left(\frac{Z_2 - Z_1}{Z_2 + Z_1}\right)^2, \qquad (2.2.1)$$

where R is the reflection coefficient at the cornea/gas boundary, and Z_1 and Z_2 are the acoustic impedances of the two materials (412 and 1.50 x 10^6 $\frac{Pa \cdot s}{m}$ for air and cornea, respectively). This results in a reflection coefficient of 0.999 for the acoustic wave reaching the bubble within the cornea. The acoustic radiation pressure can be written as

$$P = (1 + R^2)\frac{I}{c}, \qquad (2.2.2)$$

where 'R' is the reflection coefficient, 'I' is the average acoustic intensity, and 'c' is the speed of sound [Elrod 1989, Angelsen 2000]. Since the reflection coefficients is close to unity in the case of a bubble in the cornea, equation 2.2.2 reduces to

$$P = 2\frac{I}{c}. \qquad (2.2.3)$$

The acoustic radiation pressure imparts a force normal to cross-sectional area of the microbubble. The acoustic radiation force is given by

$$F = \frac{2I\pi a^2}{c}, \qquad (2.2.4)$$

where 'a' is the bubble radius. The intensity of the focused ultrasound can be experimentally determined using a calibrated hydrophone, while the bubble radius can be measured directly using a microscope. Next we must consider the movement of the bubble in response to the acoustic radiation force and the relationship between the displacement and elasticity.

The response of a viscoelastic tissue mimicking phantom to an acoustic radiation force impulse was described using the classic Voigt model [Walker 2000]. Here we use this model as a simplified illustration of the bubble response to an acoustic radiation force. The Voigt model consists of an elastic element in parallel with a viscous or damping element. The model proposes that the force applied to the tissue is opposed by an elastic force proportional to displacement and a viscous force proportional to the velocity of displacement. The differential equation is formulated as

$$F = \gamma\frac{dx}{dt} + kx \qquad (2.2.5).$$

In equation 2.2.5, F is the applied force, x is the displacement, γ is the drag coefficient, and k is the spring coefficient. Solving the differential for a force, F, applied at t=0 gives

$$x(t) = \frac{F}{k}[1 - \exp\left(-\frac{t}{\tau}\right)], \qquad (2.2.6)$$

where $\tau = \gamma/k$ and is the relaxation time constant. The bubble is displaced rapidly at first then the displacement tapers off at some point depending on the value of tau. Maximum displacement happens once velocity has gone to zero and there are no longer viscous forces (t>> τ); only the spring force remains giving

$$x_{max} = \frac{F}{k}. \qquad (2.2.7)$$

The maximum displacement of the bubble is proportional to the applied acoustic radiation force and inversely proportional to the spring constant, or Young's modulus. Once the acoustic radiation force is turned off, the bubble should return to the original position following an exponential decay,

$$x(t) = \frac{F}{k} \exp\left(-\frac{t}{\tau}\right). \qquad (2.2.8)$$

This simple model gives a good insight into the general expected behavior of a bubble embedded in an elastic medium in response to an acoustic force. Figure 2.1 shows the expected path a bubble in a viscoelastic medium in response to an acoustic radiation force. The figure was generated in MATLAB using equations 2.2.6-2.2.8 and arbitrary constant values.

Despite the utility of the Voigt model in understanding the general behavior of a viscoelastic medium in response to a force impulse, the behavior of a bubble in an acoustic field requires special consideration. The effect of radiation force on solid spheres embedded in a viscoelastic medium was studied and showed that the movement of the sphere could be used to calculate local elastic properties [Oestreicher 1951]. More recently the formation and oscillation of bubbles under acoustic fields has been investigated [Jong 2002, Karpiouk 2009, Tse 2004]. The displacement of a bubble in an elastic, homogeneous, isotropic incompressible medium in

response to an acoustic radiation force was specifically investigated in the linear approximation [Ilinski 2005]. Unlike a bubble within a liquid, a bubble in an elastic medium will only be displaced as long as the radiation force is greater than the resistive forces arising from the elastic properties of the tissue. The displacement of the bubble in polar coordinates can be written as:

$$x_r = \frac{F_r \cos(\theta)}{4\pi E a} \qquad (2.2.8)$$

$$x_\theta = \frac{F_r \sin(\theta)}{8\pi E a}. \qquad (2.2.9)$$

In this research we apply the acoustic radiation force normal to the surface of the cornea and measure the axial displacement of the bubble surface. In this respect, we are interested in the radial component of the displacement where $\theta = 0$. Thus equation 2.2.9 is reduced to zero while the equation for displacement along the radial axis is reduced to:

$$x_r = \frac{F_r}{4\pi E a}, \qquad (2.2.10)$$

where 'x' is the maximum displacement of the bubble, F_r is the acoustic radiation force, E is the elastic modulus of the cornea, and 'a' is the radius of the bubble. Substituting equation 2.2.4 in for the acoustic radiation force F_r and rearranging to solve for E, we arrive at the elastic modulus acquired from an ARFEM measurement:

$$E = \frac{Ia}{2c x_{max}}. \qquad (4.11)$$

The intensity 'I' and bubble radius 'a' are calibrated beforehand, 'c' is defined as the speed of sound in water (1500 m/s), while the bubble radius and maximum displacement, x_{max}, is measured experimentally. In this way we can calculate the Young's modulus of the cornea. The bubble radius can either be directly measured optically or a relation between bubble radius and

the amplitude of the bubble signal can be derived. Maximum bubble displacement will be in the range of 10 μm.

2.3 Methods

2.3.1 The ARFEM System

Figure 2.2 illustrates the schematics of the ARFEM system. A femtosecond laser is focused into the focal volume of a dual element, confocal ultrasound transducer. A laser pulse creates a bubble at the desired location in the cornea or gelatin sample. Next, focused ultrasound from the force generating element pushes on the bubble while the inner tracking element monitors the axial position of the bubble with an A-scan. The sample chamber is mounted to a 3-D micro-stage enabling precise positioning of the bubble within the cornea. The laser and ultrasound foci remain fixed and aligned with each other.

A commercial Ti:sapphire femtosecond laser (Coherent Inc., Santa Clara, CA) is used to create microbubbles in the samples. The laser produces 130 fs pulses at 800 nm wavelength. The beam is focused through a 0.3 NA objective with a working distance of 40 mm. Pulse energy of 80μJ is used for bubble creation. The ultrasound transducer used to probe the microbubble was custom built to our specifications by the NIH Resource Center for Ultrasonic Transducer Technology at the University of Southern California. The transducer consists of two confocal elements. The bubble tracking element (inner) is a 1-3 PZT crystal with a diameter of 15 mm and has a center frequency of 17 MHz with an f-number of 2.9. The HIFU, acoustic radiation force generating element (outer) is a PZT-4 crystal with a 30 mm diameter and has a center frequency of 1.7 MHz with an f-number of 1.4. Figures 2.3 and 2.4 show the frequency response of the tracking and force elements, respectively. Both have a focal length of 41 mm. The spatial peak, pulse average intensity (I_{sppa}) of the force generating element is 125 Watts/cm^2.

Figure 2.5 shows the wiring schematic for synchronization of inner and outer ultrasound elements, as well as the digitizing board. Synchronization between the force element, imaging element, and digitizing board is necessary to ensure that the position of the bubble is measured exactly when the force is turned off. The tracking element is driven by a commercial pulser-receiver (Panametrics Model 5072PR, Waltham, MA) at a pulse repetition frequency of 5 kHz, giving one A-scan every 200 µs. The pushing element is driven by an arbitrary function generator (Agilent Technologies Model 3314a, Palo Alto, CA) feeding a 50 dB amplifier (ENI Model 240L, MKS Instruments, Wilmingtom, MA). RF signals from the tracking element are captured by a digitizing board (Agilent Technologies, Palo Alto, CA) on a PC sampling at 100 MS/s. All components are synchronized to a 10 MHz master clock. Furthermore, the A-scan tracking pulses are synchronized with an additional tunable delay to ensure that the tracking pulse train can be moved with respect to the acoustic radiation force.

2.3.2 Gelatin Phantom Construction

Gelatin phantoms were tested to validate the ARFEM technique and were used in all subsequent experiments to secure and acoustically couple the corneal samples to the transducer. For validation purposes three collagen based gelatins (Type-A, Sigma-Aldrich, St. Louis, MO) phantoms were tested: 5%, 7.5%, and 10% by weight. The gelatin was dissolved in degassed, distilled water and brought to just below boiling to remove any air bubbles. The gelatin was then poured into the sample chamber and refrigerated for no less than 6 hours. The gels were allowed to reach room temperature before measurements took place.

ARFEM measurements were conducted in gelatin phantoms and compared against needle indentation measurements in the same phantoms. In this method a flat ended cylinder connected

to a load cell is used to indent the sample. The elastic modulus is calculated based on the recorded stress-strain relationship and the geometry of the indenting cylinder [McKee et al. 2011]. Measurements were made in gels with concentration of 5, 7.5, and 10 percent by weight.

2.3.3 Signal Processing/data analysis

A typical measurement contains three distinct portions: 1 ms before the acoustic force is applied, the 2 ms during the acoustic force during which the bubble is displaced, and between 4 and 6 milliseconds after the acoustic force is turned off as the bubble returns to its original position. The raw, 1-D RF data is sectioned and stacked into a 2-D array, where each column represents a single A-scan. A single A-scan represents the time of flight of the ultrasound pulse from the transducer, to the surface of the bubble, and back to the transducer. The time of flight is directly related to the axial distance of the bubble surface from the transducer surface. The pulser-receiver triggers the A-scan at a 5 kHz pulse repetition frequency, resulting in a 1-D image of the cornea and bubble in every 200 μs. Thus, the resulting M-scan describes the time evolution of the bubble movement in 200 μs steps. A typical M-scan measurement is presented in Figure 2.6. An M-scan is a series of A-scan pulse echoes plotted as a function of time. This figure was derived from a porcine eye and is used here solely for visualization of the actual measurement. The porcine cornea is thicker and softer than the human cornea allowing for easier distinction of the anterior, posterior, and bubble surfaces. The vertical checkered band is the saturated acoustic radiation force pulse as detected by the tracking element. The figure shows the position of the anterior/posterior corneal surfaces and microbubble before, during, and after the chirped force pulse. The small inset figure shows one sample A-scan taken from the 2-D image.

The bubble is displaced in the direction of the acoustic force and returns to its original position once the force pulse is turned off.

Bubble displacement is calculated from the RF data using a 1-D phase-sensitive cross-correlation method between a reference bubble A-scan and the remaining A-scans [Lubinski et al. 1999]. The cross-correlation algorithm computes the time lag between subsequent A-scans of the bubble and compares them to the reference A-scan (original bubble position). This method is capable of subsample resolution by using phase information in the complex correlation signal. The phase zero crossing corresponds to the peak time lag between signals and is directly related to the displacement by $y = tc/2$, where 'y' is displacement, 't' is the time lag, and 'c' is the speed of sound in water (1500 m/s). In addition to imparting a force on the bubble, the force also induces a strain in the gelatin medium containing the cornea. This is analogous to the strain induced in ARFI strain imaging. In the case of ARFEM, this strain artificially inflates the displacement of the bubble and must be accounted for. The strain of the gelatin is estimated by tracking the surface of the gelatin and subtracting its displacement from that of the bubble.

Differences in time of flight of the ultrasound pulse correspond to different depths of the reflector. Ultrasound transducers with center frequencies between 7 and 20 MHz have been successfully used to detect depth differences of a single micron [Erpelding et al. 2007, Roth et al. 1999]. Ultrasound pachymeters within this frequency range have a reported micron depth detection resolution (Reichert iPac, Depew, NY). The transducer used in this research has similar specifications and was capable of measuring equally minute time of flight differences.

2.4 Gelatin Phantom Results

Measurements were first conducted in gels ranging from 5 to 10% gelatin by weight. Figure 2.7 compares ARFEM and needle indentation elasticity measurements in gels of varying concentration. At least 5 bubbles were measured in each gelatin phantom. ARFEM measured average elastic moduli with standard deviations of 0.82 ± 0.09 kPa, 1.09 ± 0.04 kPa, and 1.59 ± 0.16 kPa in the 5, 7.5, and 10 percent gels, respectively. The indentation method measured 1.11 ± 0.03 kPa, 2.28 ± 0.08 kPa, and 3.45 ± 0.12 kPa for the 5, 7.5, and 10 percent gels. Both methods show a linearly increasing elasticity with increasing concentration. Figure 2.8 shows the averaged displacement paths of the bubbles during the ARFEM measurements. As expected, maximum bubble displacement are inversely proportional to the elasticity of the surround medium. Bubbles are able to travel further in softer gels before the acoustic radiation force is balanced by resistive forces within the surrounding gelatin. Figure 2.9 shows the stress-strain curves obtained via the indentation method. As expected, the gels of higher gelatin concentration possess a steeper stress strain curve indicating a higher elastic modulus. The curve is linear for small strains.

Separate measurements were performed to investigate the effect of push element driving voltage on bubble displacements. Figure 2.10 shows the maximum displacement in gels of 10%, 15%, and 20% concentrations for linearly increasing driving voltage, with all other parameters being held constant. Displacement ranged from 5 to 45 µm. Each data point represents the average of 10 measurements in 2 separate bubbles. There are no measurements in the 10% phantom at 100 and 125 mV because the gel yielded and the bubbles were translated through the gel to new permanent locations instead of being elastically displaced. Similarly, there was no detectable displacement at 25 mV in the 15 and 20% phantoms. Bubble displacement increases linearly for linearly increasing driving voltage and thus acoustic intensity.

2.5 Pilot Porcine Cornea Measurement

Measurements were performed in a pig cornea to determine whether measurements were possible inside of the cornea. Figure 2.11 show the average relaxation path of 5 bubbles made within the porcine cornea. The bubbles were all in the central/posterior cornea at the same axial depth in a cluster inside of a square millimeter. The average displacement of the bubbles was 35 ± 2 μm. This result demonstrates the ability of the ARFEM system to create, displace, and track bubbles within the corneal environment.

2.6 Discussion

Traditional acoustic radiation elasticity techniques are complicated by the focal volume of the high intensity ultrasound element being used. The complex strain field within this volume is non homogeneous and thus introduces difficulties when calculating elastic properties. Furthermore, the elasticity calculated is representative of the entire interrogated volume, wich is difficult to define and somewhat arbitrary. This volume depends directly on the geometry and properties of the ultrasound itself. Focal diameters of 1 mm are not uncommon [Xu et al. 2014]. This is especially true of low frequency high intensity ultrasound. For example, the high intensity element used in this research is very broadly focused. Figure 2.12 shows the transverse intensity acoustic profile as a function of radial distance away from the geometric focal point (at the focal plane 41 mm away from the transducer). At 100 μm on either side of the focal point, the acoustic intensity is nearly 100% of the maximum value. Even at 0.5 mm on either side of geometric focal point the acoustic pressure is still 60% of the maximum value. Bubble based ARFEM is unique in its ability to measure highly localized elasticity which is essentially localized despite

the broad focusing of the high intensity element. In the vicinity of the bubble the acoustic field can be assumed to be uniform, thus the bubble acts as a point like source for the elasticity measurement. The difference between absorption and bubble based techniques is illustrated in Figure 2.13. It is easy to see the complex strain field caused by the absorption based technique. Acoustic radiation force acts upon a large and ill defined volume of tissue whereas in the bubble based technique the acoustic force and resultant displacement is limited to the location of the bubble.

ARFEM measurements in gelatin samples of varying concentration were encouraging. Bubble displacements followed the paths similar to those predicted by the Voigt model. Displacements magnitude was inversely proportional to gelatin concentration and also linearly proportional to applied voltage as shown in Figure 2.10. ARFEM measurements were in good agreement with previously published elastography techniques as shown in Figure 2.7. While there are some small discrepancies in the absolute values, both needle indentation and ARFEM show the same linear dependence of elasticity on gelatin concentration. The small discrepancies in absolute value may be explained by the fact that needle indentation measurements are performed on the surface of the gel, while ARFEM is performed inside the material. The exposure of the gelatin surface to ambient air during micro-indentation may also have some effect. Despite this, the elasticity values between the two methods did not vary by more than a factor of two. As mentioned in section 1.2, it is not uncommon for different elasticity techniques to return drastically different results in the same medium. The reported values for corneal elasticity easily span three orders of magnitude depending on the technique used [Winkler et al. 2011, Nyquist 1968, Hoeltzel 1992, Zeng 2001, Wang et al. 1996]. Micro-

indentation was chosen as a comparative method for our purposes because the displacement strain induced is on the order of tens of microns, which is very similar to ARFEM.

2.7 Conclusions

The results of the ARFEM study in gelatin phantoms and the pilot measurement in a porcine cornea demonstrate the potential of ARFEM for measuring human corneal elastic properties. ARFEM provided reliable results in gelatin phantoms which were comparable to established methods. Bubble displacement was inversely proportional to local elasticity, while the displacement paths were predictable and adhered to the Voigt model for viscoelastic tissue.
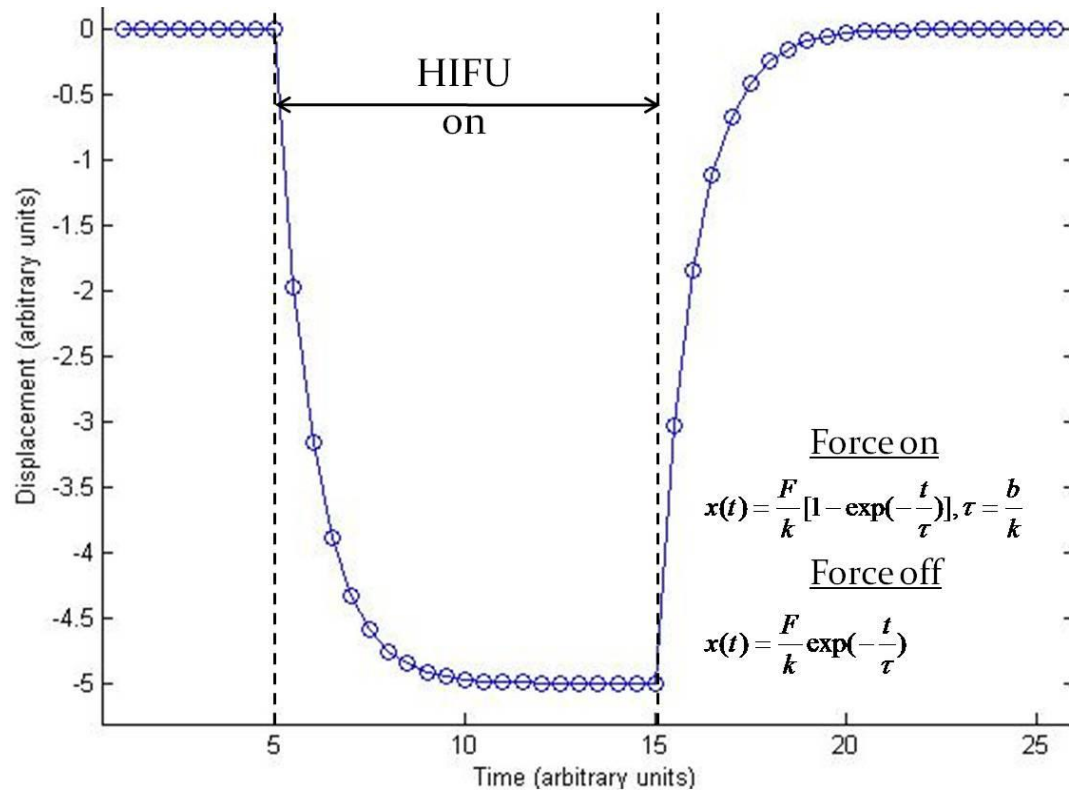
Figure 2.1: Theoretical displacement path of a bubble in a viscoelastic medium in response to a acoustic radiation force.
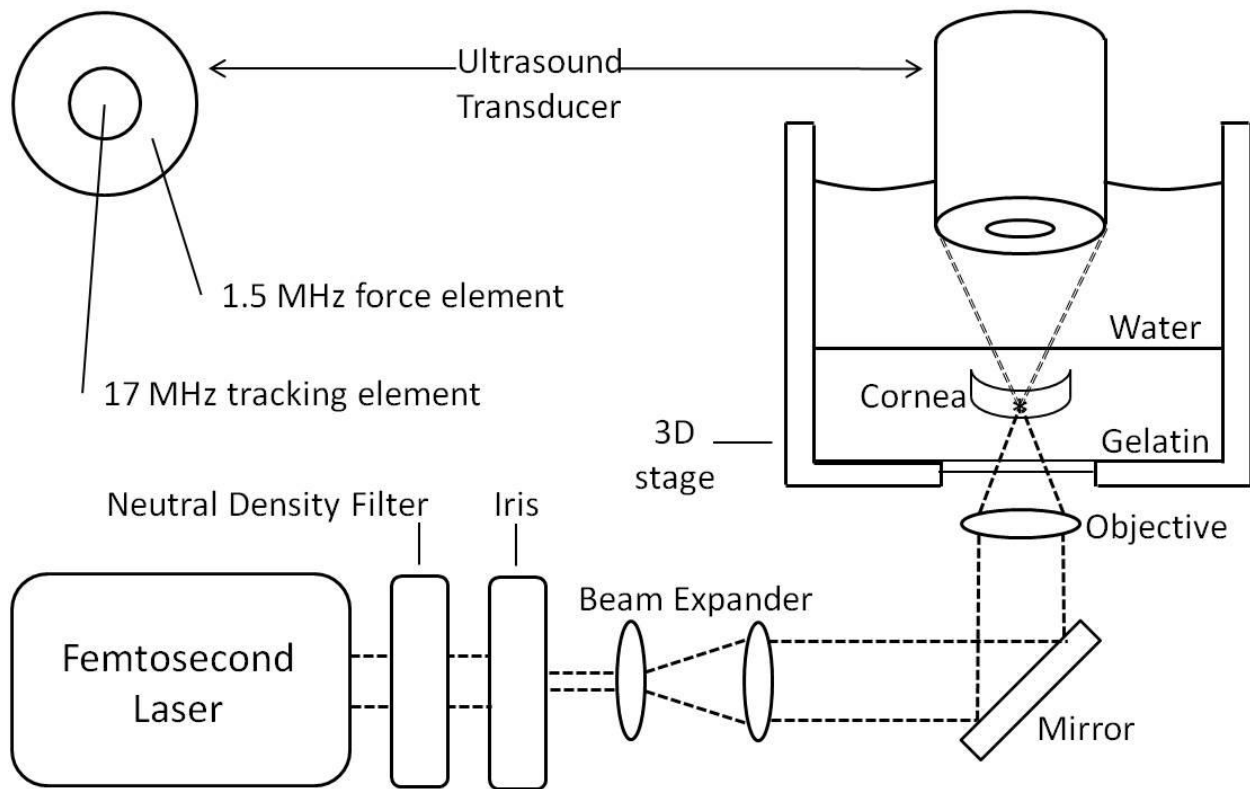
Figure 2.2: Experimental setup. The corneal sample and acoustic tank are placed on a 3D positioning stage that can move independent of the laser and transducer.
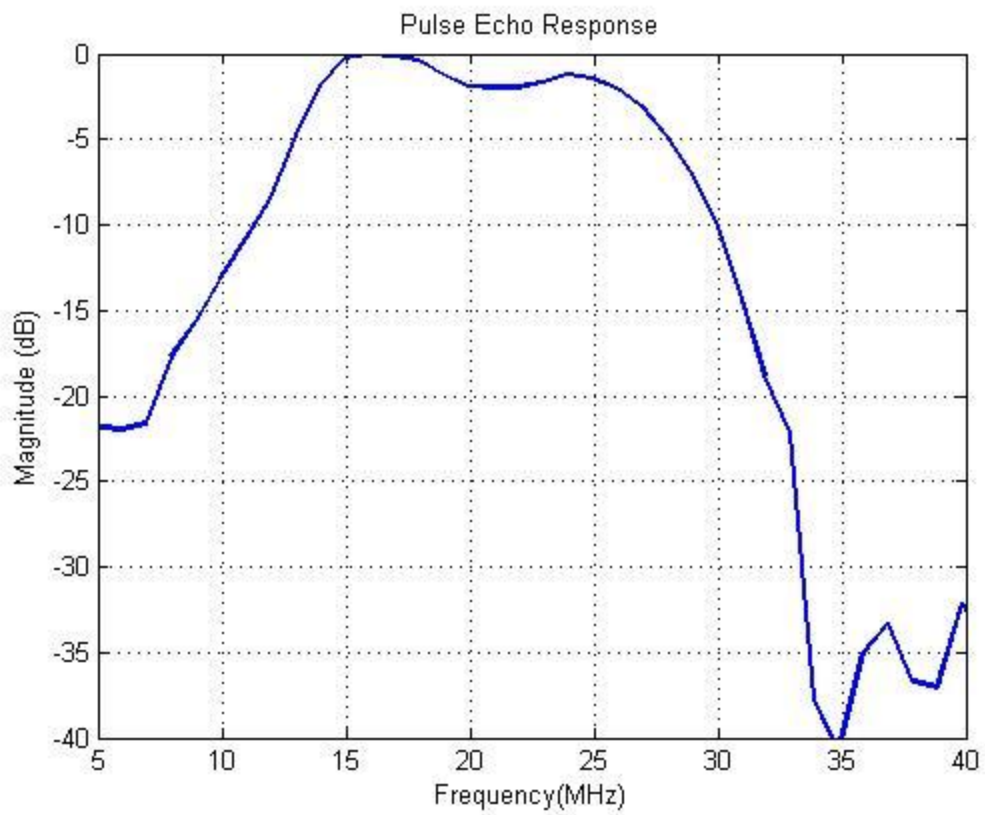
Figure 2.3: Frequency response of the inner tracking element. (center frequency = 17Mhz)
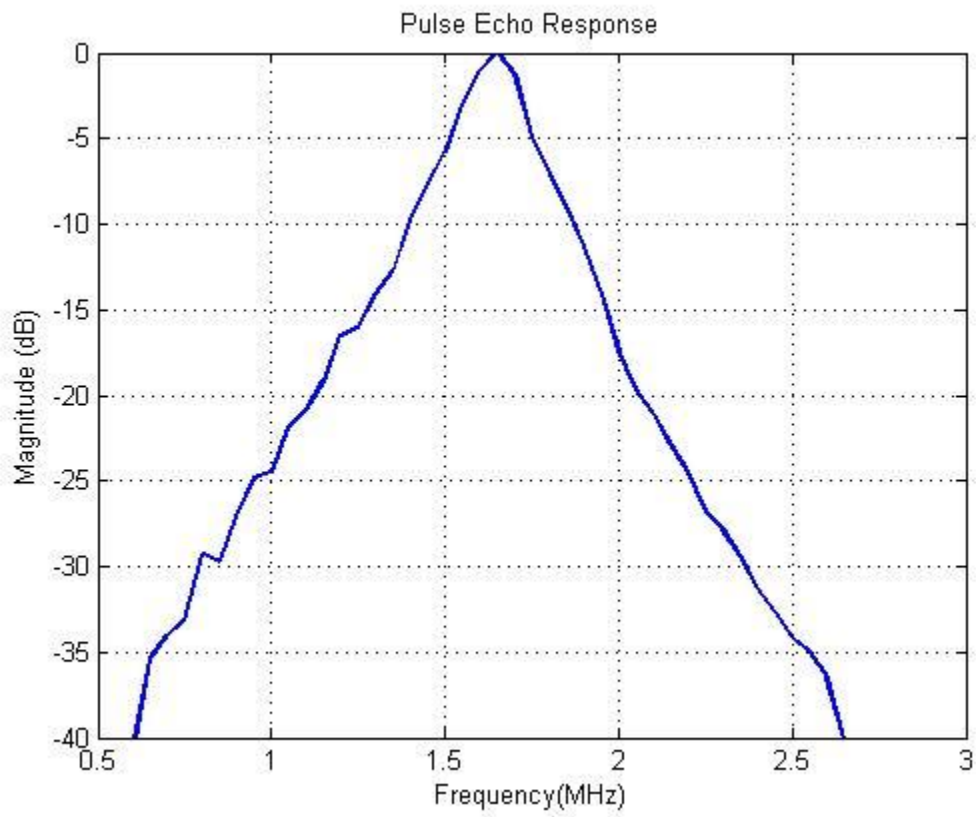
Figure 2.4: Frequency response of the outer force generating element. (center frequency = 1.7 Mhz)
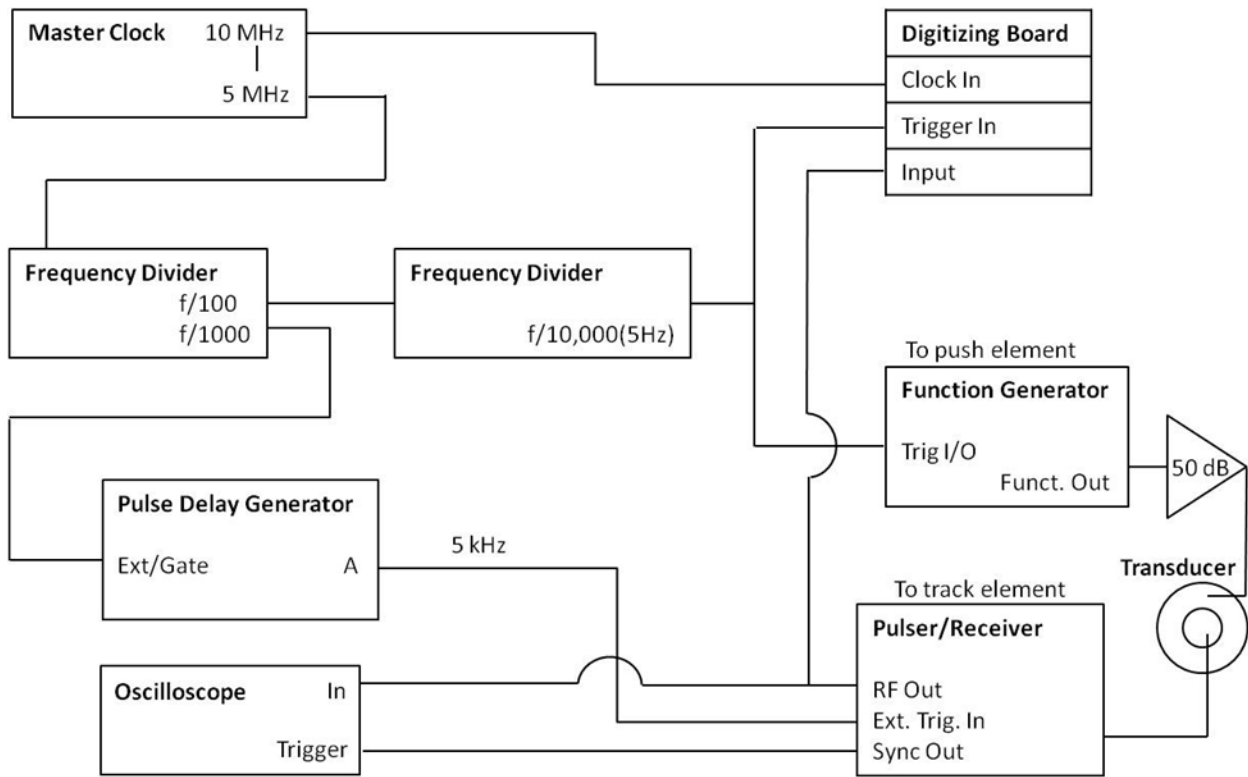
Figure 2.5: Electronics synchronization wiring diagram. All equipment is synchronized to a 10 MHz master clock. The digitizing board samples the RF signal at 100 MHz.
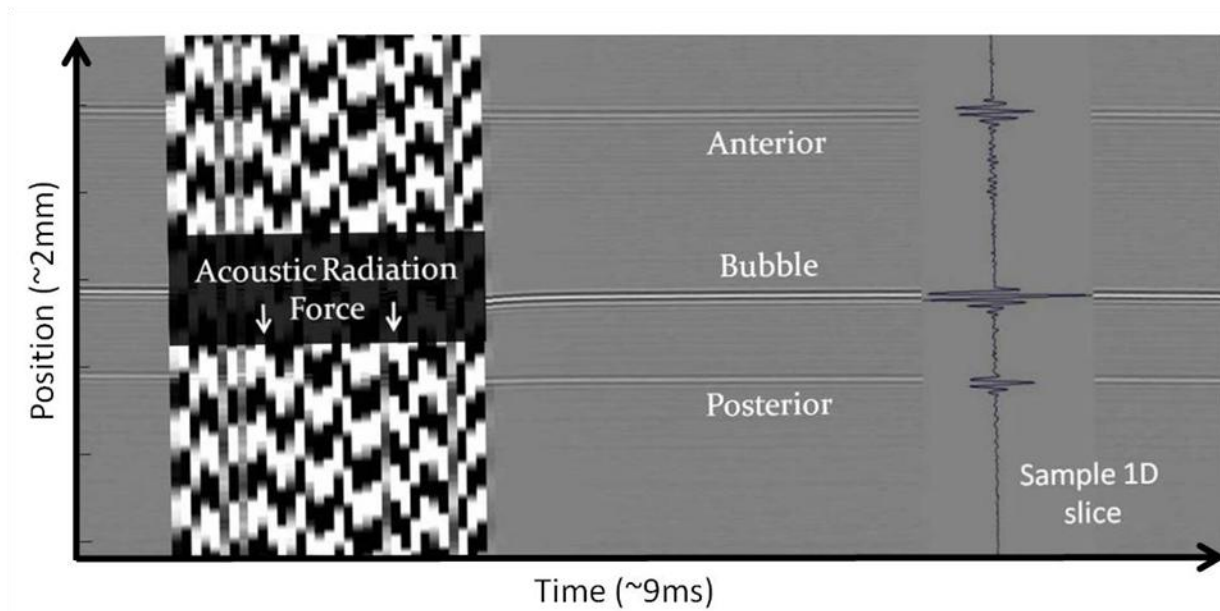
Figure 2.6: Sample M-scan from a swollen porcine cornea showing the position (y-axis) of the bubble as a function of time (x-axis) as well as the force pulse (vertical band). The y-axis spans about 2 mm, while the x-axis spans 9 ms. The sample 1D slice represents just one of the A-scans at 7 ms time delay taken from the 2D image.
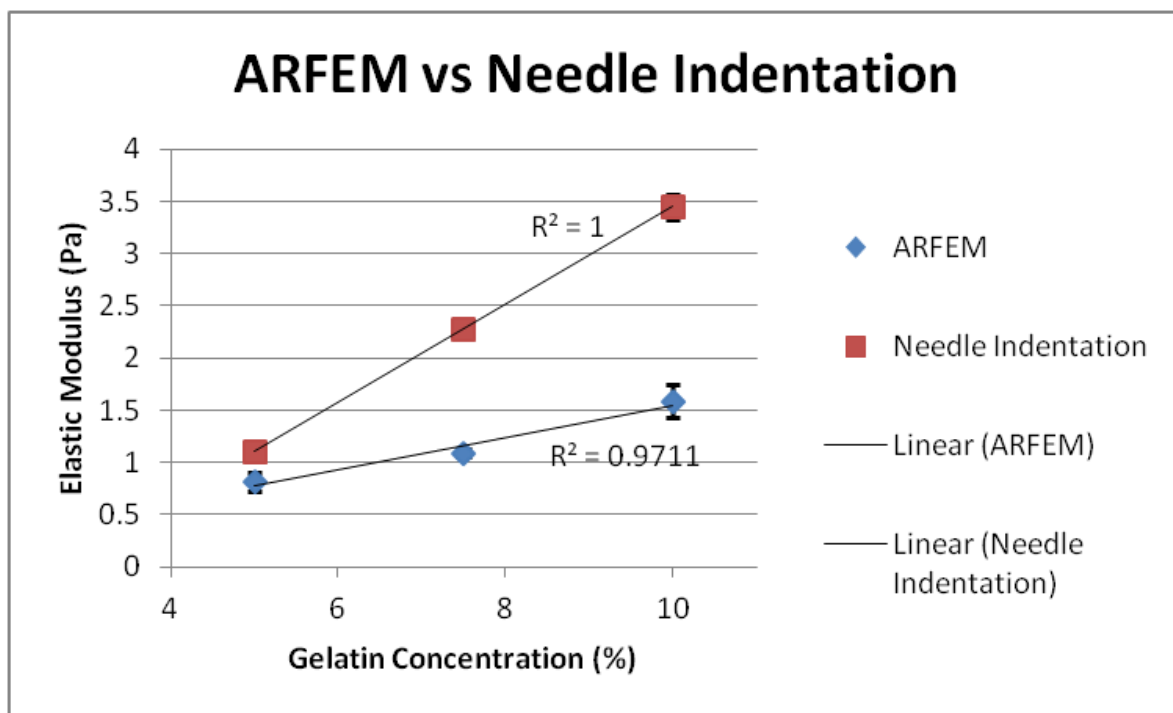
Figure 2.7: Elastic modulus of 5%, 7.5%, and 10% gels as measured by ARFEM and needle indentation. The solid lines represent linear fit to the data.
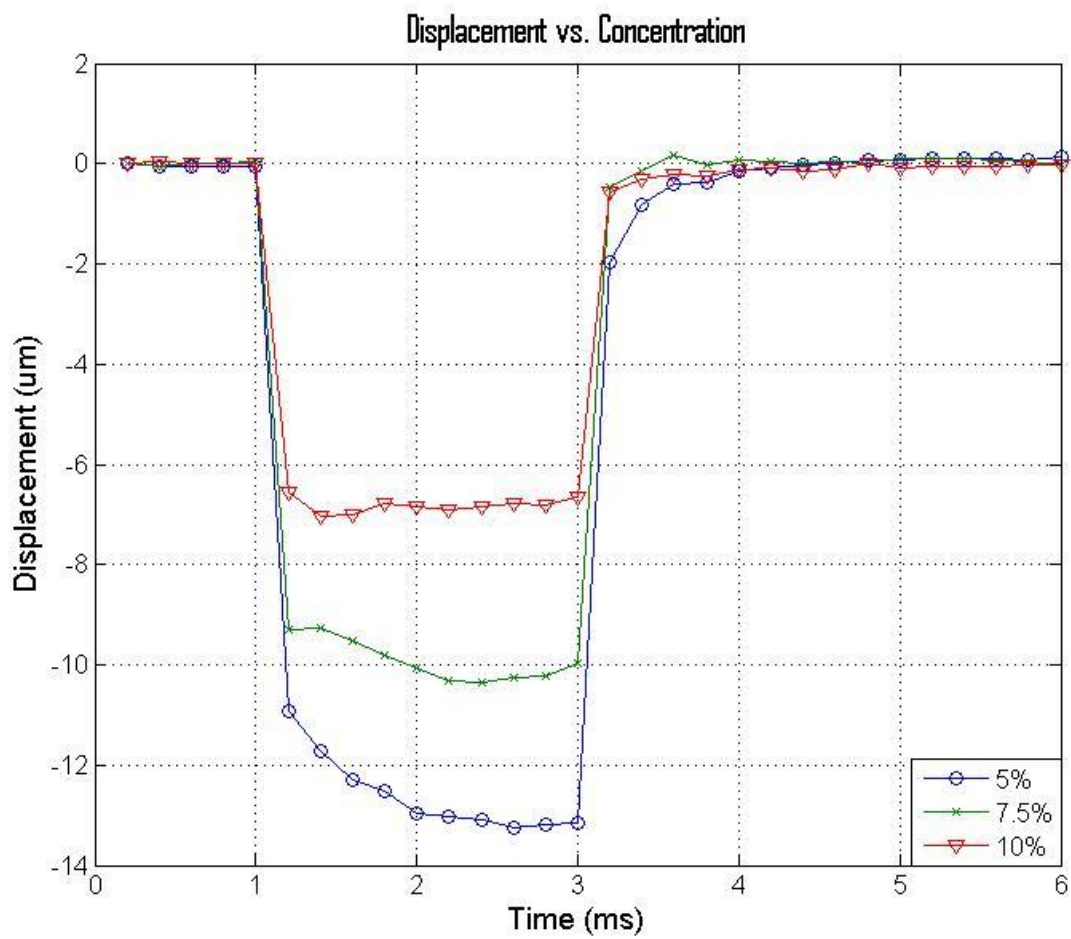
Figure 2.8: The averaged displacement paths in gelatin phantoms of varying concentrations.
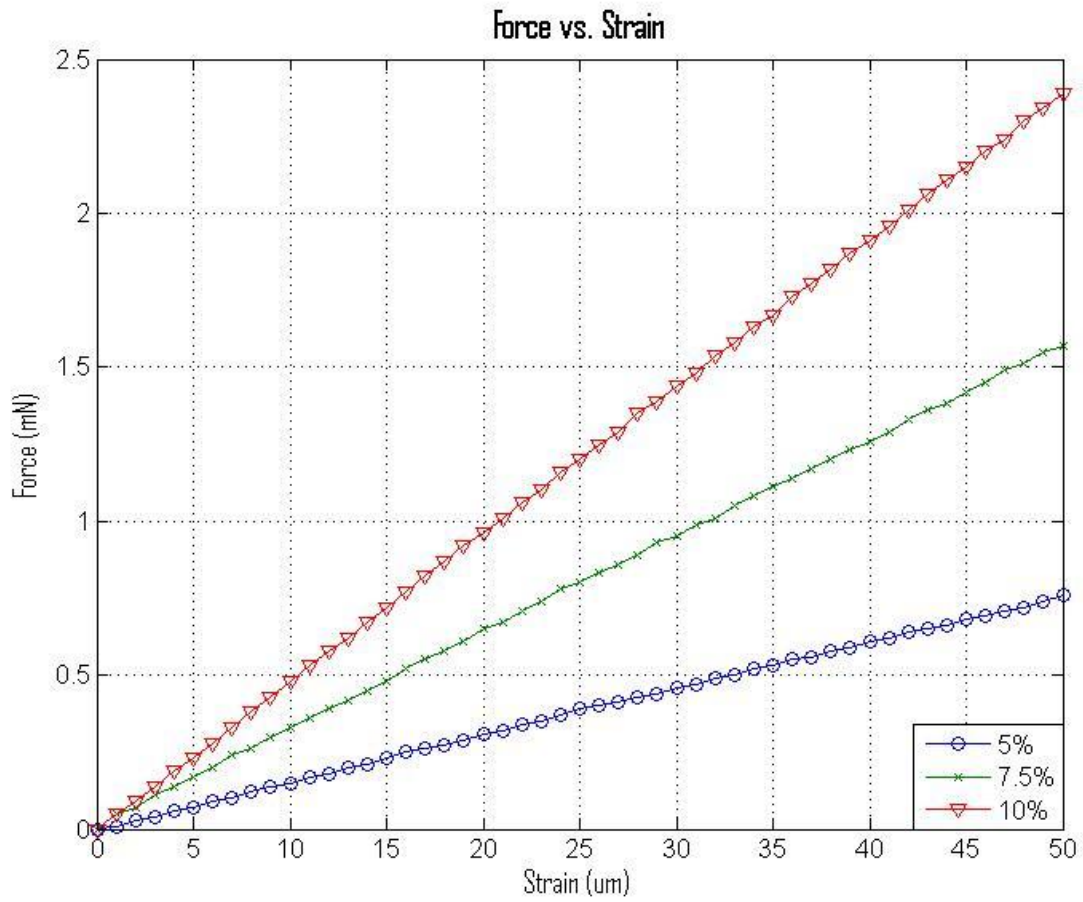
Figure 2.9: Stress-Strain curves for phantoms of varying gelatin concentrations using micro-indentation. Steeper slopes indicate higher elastic modulus.
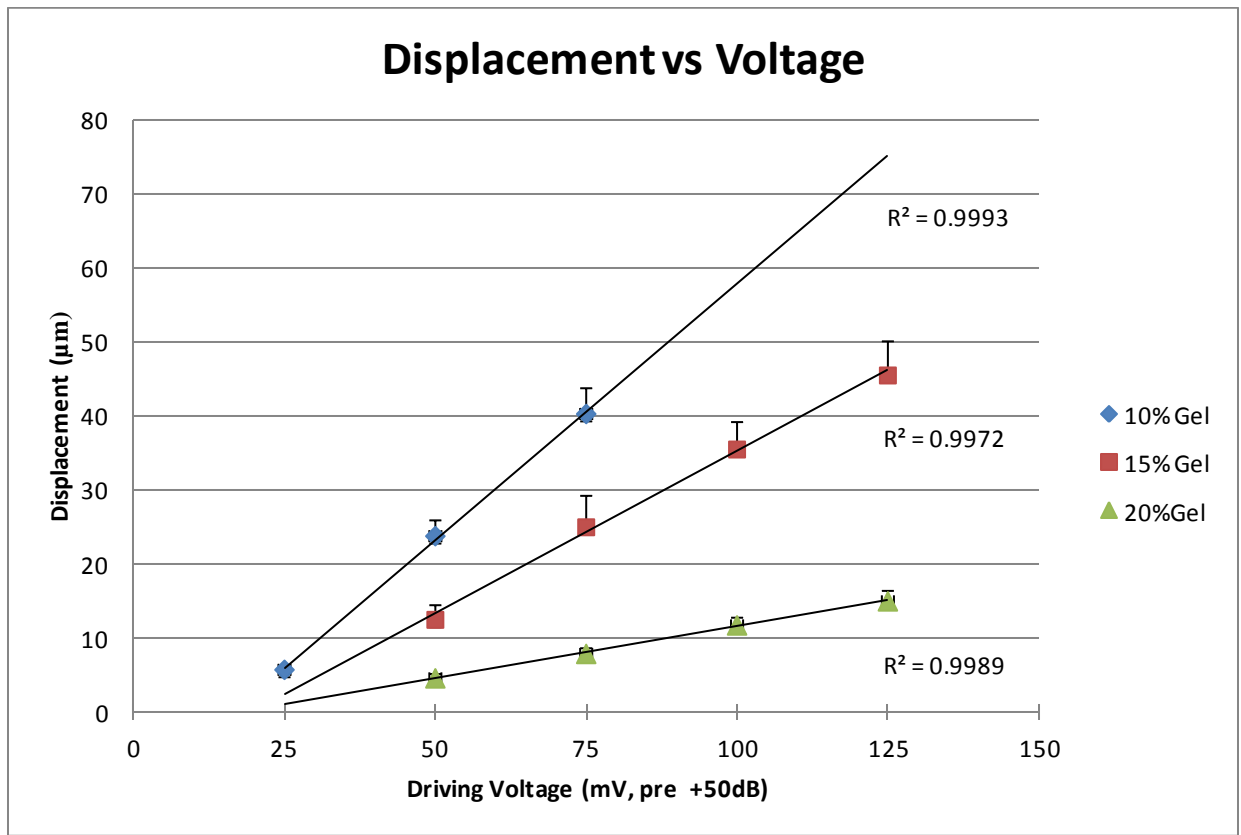
Figure 2.10: Maximum displacement in gels of 10%, 15%, and 20% concentrations for linearly increasing driving voltage.
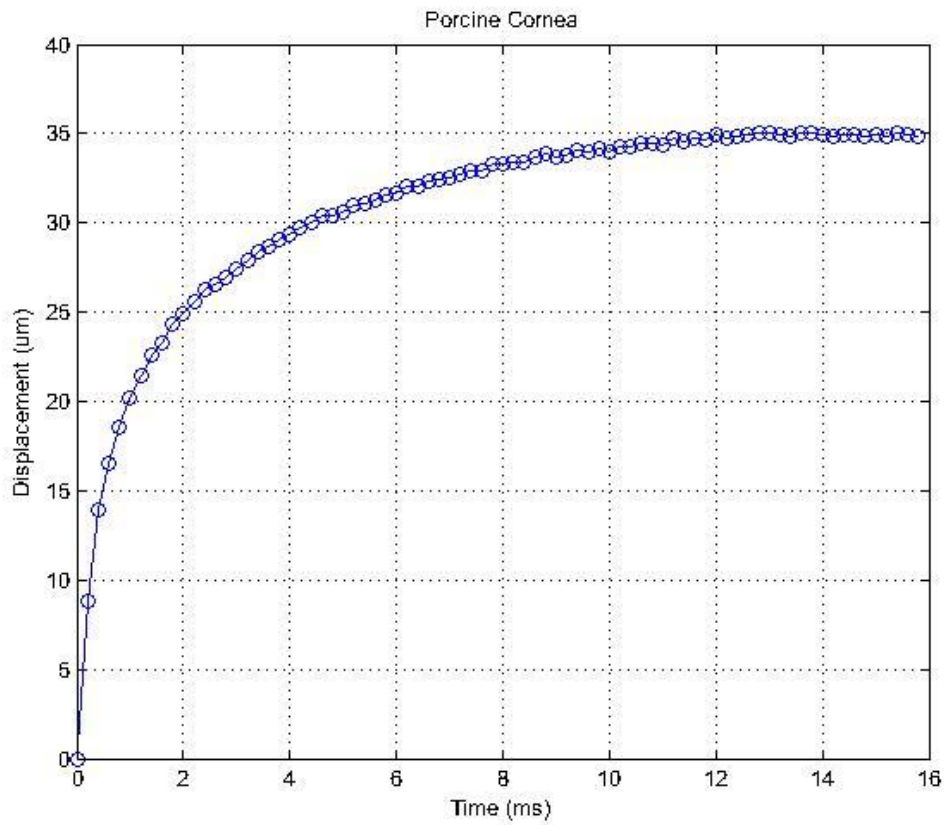
Figure 2.11: Averaged relaxation path for 5 bubbles in the hydrated porcine cornea. The average displacement is 35 μm ± 2 μm.

Figure 2.12: Traverse acoustic intensity profile in the focal plane of the transducer used in this research.

Figure 2.13: Absorption based techniques apply to a large volume, resulting in a complex strain field. Bubble based acoustic techniques such as ARFEM result in a localized high amplitude force on the bubble itself.

2.8 References

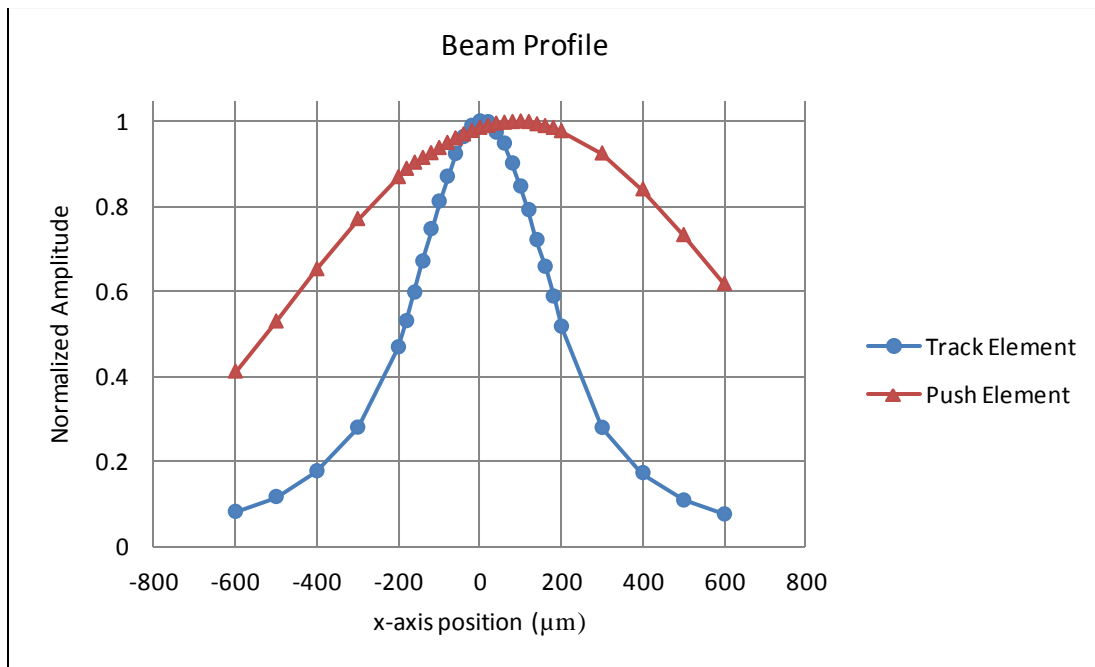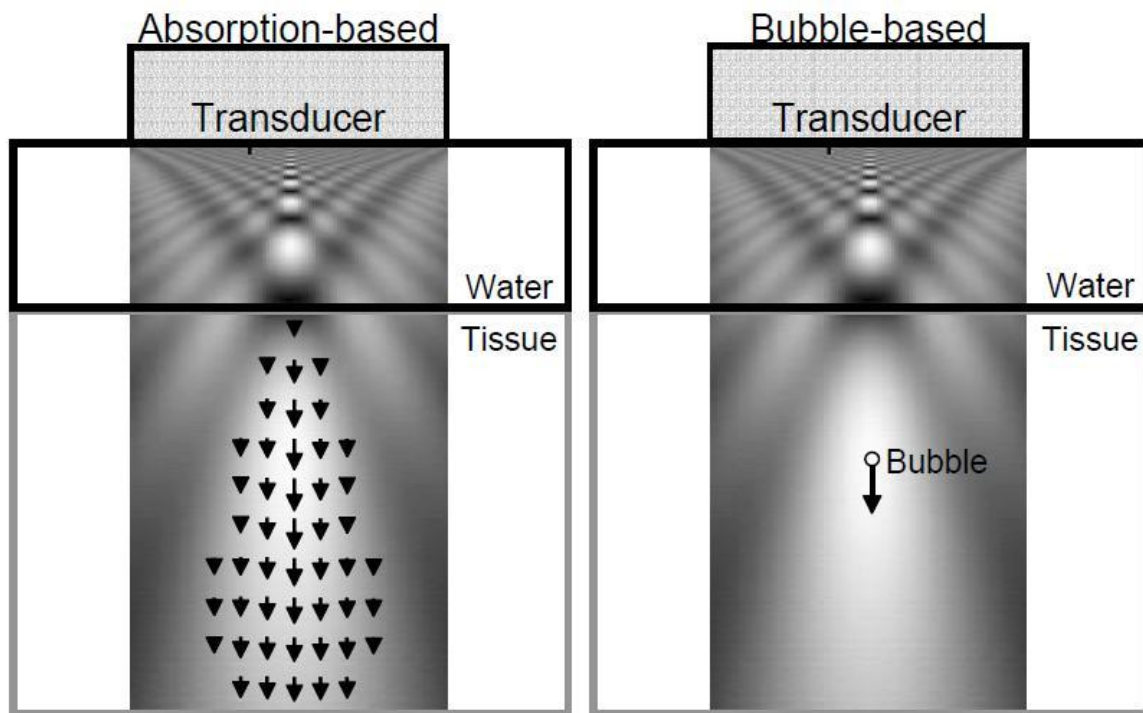Andrei B. Karpiouk ; Salavat R. Aglyamov ; Frederic Bourgeois ; Adela Ben-Yakar ; Stanislav Y. Emelianov; Ultrasound characterization of cavitation microbubbles produced by femtosecond laser pulses. Proc. SPIE 7175, Optical Interactions with Tissue and Cells XX, 717512 (February 12, 2009);

Angelsen BAJ. Ultrasound imaging. Trondheim, Norway: Emantec, 2000.

Bercoff, J.; Tanter, M.; Fink, M. "Supersonic shear imaging: a new technique for soft tissue elasticity mapping," Ultrasonics, Ferroelectrics and Frequency Control, IEEE Transactions on , vol.51, no.4, pp.396-409, April 2004.

De Jong, Nico, Ayache Bouakaz, and Peter Frinking. "Basic acoustic properties of microbubbles." Echocardiography 19.3 (2002): 229-240.

Elrod SA, Hadimioglu B, Khuri-Yakub BT, et al. Nozzleless droplet formation with focused acoustic beams. J Appl Phys. 1989;56(9):3441–3447.

Erpelding T, Hollman K, O'Donnel M. "Bubble-based acoustic radiation force elasticity imaging." IEEE Trans Ultrason Ferroelectr Freq Control. 52:971-979. 2005.

Erpelding, T. N., Hollman, K. W., & O'Donnell, M. (2007). Mapping age-related elasticity changes in porcine lenses using bubble-based acoustic radiation force. *Experimental eye research*, *84*(2), 332-341. 2007.

Glezer EN, Schaffer CB, Nishimura N, Mazur E. "Minimally disruptive laser induced breakdown in water." Opt. Letter 1997. 22(23):1817-1819. 1997.

H. L. Oestreicher, ''Field and impedance of an oscillating sphere in a viscoelastic medium withan application to biophysics,'' J. Acoust. Soc. Am. 23, 707–714. 1951.

Hjortdal J O. Extensibility of the normo-hydrated human cornea. Acta ophthalmologica Scandinavica. 73. 12-17, 1995.

Hjortdal J O. Regional elastic performance of the human cornea. J. Biomechanics. 29:931-942. 1996

Jue B, Maurice D. The mechanical properties of the rabbit and human cornea, Journal of Biomechanics, Volume 19, Issue 10. Pages 847-853. 1986.

Juhasz T, Kastis G, Suarez C, Bor Z, Bron W. Time resolved observation of shock waves and cavitation bubbles generated by femtosecond laser pulses. Lasers IN Surgery and Medicine. 1997. 19:23-31. 1997.

Kennedy PA, Boppart SA, Hammer DX, Rockwell BA, Noojin GD, Roach WP. "A firstorder model for computation of laser-induced breakdown thresholds in ocular and aqueous media: part II comparison to experiment." IEEE J Quantum Electron 1995b; 31(12):2250-2257. 1995.

Loesel FH, Niemz MH, Bille JF, Juhasz T. "Laser-induced optical breakdown on hard and soft tissues and its dependence on the pulse duration: experiment and model." IEEE J Quantum Electron 1996; 32(10):1717-1722. 1996.

Mikula, E., Hollman, K., Chai, D., Jester, J. V., & Juhasz, T. (2014). Measurement of Corneal Elasticity with an Acoustic Radiation Force Elasticity Microscope. Ultrasound in medicine & biology, 40(7), 1671-1679.

Nightingale, K.; Palmeri, M.; Bouchard, R.; Trahey, G.; , "Acoustic radiation force impulse imaging: a parametric analysis of factors affecting image quality," Ultrasonics, 2003   IEEE Symposium on , vol.1, no., pp. 548- 553 Vol.1, 5-8 Oct. 2003.

Roth D, Whalen M, Hendricks L, Bodis J. "Using High Frequency Focused Water Coupled Ultrasonic Pulses for 3D Surface depression profiling." NASA Center for Aerospce Information. NASA/TM-1999-209268. 1999.

Sarvazyan AP, Rudenko OV, Swanson SD, Fowlkes JB, Emelianov SY. "Shear wave elasticity imaging: a new ultrasonic technology of medical diagnostics." Ultrasound Med Biol. 24(9):1419-35. 1998.

Schaffer C, Nishimura N, Glezer E, Kim A, Mazur E. "Dynamics of femtosecond laser-induced breakdown in water from femtoseconds to microseconds." Opt Express. 2002 Feb 11;10(3):196-203. 2002.

Shin T, Vito R, Johnson L, Bernard E. McCarey. The distribution of strain in the human cornea. Journal of biomechanics . volume 30 issue 5 Pages 497-503. 1997.

Tanter M, Touboul D, Gennisson JL, Bercoff J, Fink M. "High-resolution quantitative imaging of cornea elasticity using supersonic shear imaging." IEEE Trans Med Imaging. 2009 Dec;28(12):1881-93. 2009.

Tse, Christine, et al. "Acoustic detection of controlled bubble creation by LIOB in tissue-mimicking gelatin phantoms." Ultrasonics Symposium, 2004 IEEE. Vol. 1. IEEE, 2004.

Ilinskii YA, Meegan GD, Zabolotskaya EA, Emelianov SY. Gas bubble and solid sphere motion in elastic media in response to acoustic radiation force. J Acoust Soc Am. 2005 Apr;117(4 Pt 1):2338-46.

Walker, Francisco J Fernandez and Laura A Negron. A method of imaging viscoelastic parameters with acoustic radiation force. Physics in Medicine and Biology. Volume 45, Number 6. 1437. 2000.

Wang S, Li J, Manapuram RK, Menodiado FM, Ingram DR, Twa MD, Lazar AJ, Lev DC, Pollock RE, Larin KV. "Noncontact measurement of elasticity for the detection of soft- tissue tumors using phase-sensitive optical coherence tomography combined with a   focused air-puff system." Opt Lett. 37(24):5184-6. 2012.

CHAPTER 3

Transducer Characterization and ARFEM Optimization

3.1 Introduction

The ARFEM system consists of an ultrasfast femtosecond laser aligned with a custom confocal transducer. The laser used was a commercial Ti:sapphire femtosecond laser (Coherent Inc., Santa Clara, CA) that produces 130 fs pulses at 800 nm wavelength. The ultrasound transducer used to probe the microbubble was custom built to our specifications by the NIH Resource Center for Ultrasonic Transducer Technology at the University of Southern California. While the commercial laser has set specifications given by the manufacturer, the custom, experimental ultrasound transducer needed to be characterized before it could be incorporated in the ARFEM system. Specifically, the output intensity needed to be measured and the focusing geometry of the confocal elements needed to be verified. It is important to know the geometry of the beam for both the acoustic radiation force element and tracking element to understand how severe an effect deviation from the focal point may have on measurements. Also, it is necessary to know the geometry of the beam for both the acoustic radiation force element and tracking element to ensure that they are confocal.

The high intensity push pulse also produced unique challenges due to the high amplitude of the signal, its interference with tracking pulse echo A-scans, and the confined, reflective nature of the acoustic sample chamber. Specifically, standing waves and noise in the A-scans due to the high intensity push needed to be addressed.

3.2 Ultrasound Transducer Calibration

3.2.1 Methods

The acoustic signal of both the tracking and force elements were measured as a function of axial (z-axis) distance and radial distance from the geometric focal point of the transducer. A calibrated needle hydrophone with a diameter of 200 μm was used to measure the beam profile characteristics and intensity output of the ultrasound transducer (Precision Acoustic, UK). All measurements were performed in degassed, distilled water. The transducer was connected to a 3-D microstage and was scanned over the hydrophone needle to determine the dimensions of the focal regions for the inner and outer elements. First, the beam profile for both elements was measured in the transverse plane. The starting point of the measurement was at the focal point of the tracking element. This point was found manually by observing the pulse echo signal on an oscilloscope.

The spatial peak, pulse average intensity of the force element was measured as a function of driving voltage. The intensity was calculated at the focus of the transducer from the recorded RF signal using equation 3.1 as outlined by American Institute of Ultrasound in Medicine. The equation is

$$I_{sppa} = \frac{\int_{t1}^{t2} v^2(t)\,dt}{10^4 \, \rho c M_L^2(f_c)PD}, \qquad (3.1)$$

where 'v' is the voltage signal from the hydrophone (V), 'ρ' is the density of water (kg/m^3), 'c' is the speed of sound in water (m/s), 'M_L' is the hydrophone sensitivity (V/Pa), and 'PD' is the force pulse duration [AIUM/NEMA 2004]. The numeric integral is calculated in Matlab using the trapezoid method for numeric integration.

3.2.2 Results

The raw voltage data was normalized for both elements. The center point for the measurements was taken to be the location when the pulse echo signal from the surface of the hydrophone was maximized. Figure 3.1 shows the transverse profile of both elements. Measurements were taken every 20 μm near the focus and every 100 μm in the periphery. As expected the tracking element is tightly focused with 40 μm on either side of its focal point within 5% of the maximum amplitude. The push element has a broader focus with about 160 μm on either side of its focal point within 5% of the maximum amplitude. More interestingly, the two elements are not exactly confocal, and are shifted by about 100 μm. Fortunately the focal region of the force generating element is broad; setting the focus of the transducer at the focal point of the tracking element only results in a roughly 2% reduction in acoustic radiation force intensity from the push element.

Figure 3.2 shows how the acoustic profile varies as the transducer is moved axially around the focal plane at 41 mm. The transducer is centered on the focal point of the tracking element in the transverse plane, corresponding to an x-axis position of 0 in figure 3.1. Again we see the focal characteristics of the outer force generating element are broader than that of the tracking element. Acoustic radiation force increases as the transducer is moved closer to the hydrophone, while tracking element amplitude drops off steeply. While not perfectly confocal, the two elements are 'close enough' due to the wide profile of the push element.

Figure 3.3 shows the spatial peak, pulse average intensity output (W/cm^2) of the acoustic radiation force generating element. The intensity increases fairly linearly with driving voltage. Measurements above the shown intensities were not performed to avoid possible damage to the

transducer. 125 W/cm^2 was determined to be adequate for the purpose of these experiments. Since the central 200 µm of the force beam profile at the focal plane was found to be uniform it is reasonable to assume that the bubble, though considerably smaller in diameter than the active element of the hydrophone, will experience the same intensity as measured by the hydrophone.

3.3 Standing Waves

Standing waves occur in an ultrasound field when incident and reflected waves interfere forming nodes and antinodes. The nodes occur where there is constructive interference and the pressure amplitude is doubled, while antinodes occur where there is destructive interference and pressure amplitude is zero. Early in this work, bubbles were observed to move in the direction opposite of the acoustic radiation force due to standing negative pressure waves. Figure 3.4 illustrates one such case. The measurement was taken in a gelatin phantom at roughly three millimeters above the bottom of the acoustic sample chamber. To reduce the effect of standing waves, swept frequency force chirps have been used instead to single frequency tone bursts when generating acoustic radiation force [Erpelding 2007]. The idea is that the incoming wave will be a different frequency and out of phase with the reflected wave. Erpelding et. al. had success with this method and was able to significantly reduce the effect of standing waves using a 300 kHz frequency sweep centered at 1.5 MHz. Another technique involves modulating a carrier frequency with random noise so that the instantaneous frequency of the pressure waves varies randomly around the center frequency of the transducer [Tang 2010]. They found that standing wave effects could be reduced by a factor of 5.6 with the random noise modulation and 3.4 with a linear frequency sweep when compared to a single frequency tone burst.

In this research, we employed a two pronged approach and completely eliminated the effect of standing waves. First, we used a force chirp as was described in the literature. The force chirp was created in Matlab and loaded into the arbitrary function generator used to drive the pushing element. The frequency was linearly swept from 1.4 MHz up to the center frequency of 1.7 MHz. Second, we used a long focal length objective lens (working distance = 40 mm) to focus the laser beam into the acoustic sample chamber. This allowed for the bubble to be created well above the optical window at the bottom of the chamber. Thus the diverging acoustic waves from the force generating element were too sparse after reflection from the bottom of the chamber to significantly interfere with incoming waves in the sample plane. In fact, based on simple geometric divergence, the acoustic intensity of the reflected wave at the focal plane should be less 1/3 of 1% of the intensity of the incoming wave.

3.4 Noise in the A-scan

The reflected high intensity force pulse causes considerable noise to arise in the A-scan. Thus the movement of the bubble during the pulse is masked. Furthermore, the 'ringing' of the force pulse even after it is turned off obstructs the movement of the bubble for a few hundred microseconds even after the force pulse is turned off. To reduce the noise in the A-scan and reveal the entire path of the bubble, a 'notched' force chirp pulse was used. Figure 3.5 shows the force pulse structure along with the embedded imaging pulse echoes. The waveform driving the force element consists of a train of 10 force pulses, each 160 µs in duration and swept in frequency from 1.4 MHz to 1.7 MHz, with a 40 µs delay between each force pulse (2 ms total). Since the A-scan operates at 5 kHz, one tracking pulse reaches the transducer ever 200 µs. Thus

the strong force pulse, which is a source of noise, is turned off when the reflected tracking pulse reaches the transducer. The adjustable delay connected to the A-scan allowed for fine tuning of the position of the pulse echoes inside the 40 µs notches. This drastically reduces noise in the A-scan and enables tracking of the bubble while it is being displaced. Figure 3.6 illustrates the effect of this method on the amount of noise in the signal. While the majority of the push force is removed from the signal via spectral filtering in post processing, the A-scan data corresponding to the position of the bubble itself is corrupted without this technique. As seen in the second panel, the position of the bubble is clear and uninterrupted when the notched force chirp is employed.

3.5 Discussion

Measurement of the acoustic profile of both the tracking and force element revealed that the confocal ultrasound transducer was not truly confocal. The focal point of the force generating element is offset from the focus of the tracking element by roughly 100 µm. Since this type of ultrasound transducer is not commercially available and lead time to build one is on the order of a full year, it was necessary to ensure that it was in fact adequate. It was determined that the offset was acceptable owing to the large diameter of the force generating beam profile. Furthermore, each ARFEM measurement was performed at the same location relative to the transducer by always performing an alignment with a sample bubble using the 5 kHz pulse echoes and the displayed signal on an oscilloscope. In this way, the measurements were always performed at the focal point of the tracking element, ensuring that acoustic intensity did not vary between measurements.

The inclusion of a frequency swept force chirp in addition to a long working distance laser objective was essential in guaranteeing stable and reproducible measurements. As seen in Figure 3.6, the notched force chirp reveals the entire path of the bubble: before, during, and after the high intensity push. It is especially important that the position at the very end of the push is visible, as this is the value used to calculate the elastic modulus. A distinct advantage of ARFEM is the high signal to noise ratio. Unlike other ultrasonic methods, the use of the femtosecond laser generated bubble as a contrast agent in the A-scan image means that the measurement is not limited to tracking endogenous speckle. The removal of push pulse noise from the signal allows us to take full advantage of the strong signal provided by the bubble.

3.6 Conclusion

Unpredictable acoustic interference in the form of standing wave was effectively removed by increasing the working distance of the laser objective and frequency sweeping the force pulse, thus greatly improving the reliability of the ARFEM device. The elimination of the noise in the bubble tracking signal caused by high intensity push pulse has un-masked the full path of the bubble in response to an acoustic radiation force. With these improvements, ARFEM has significant potential to provide high localized elasticity measurements the human cornea.
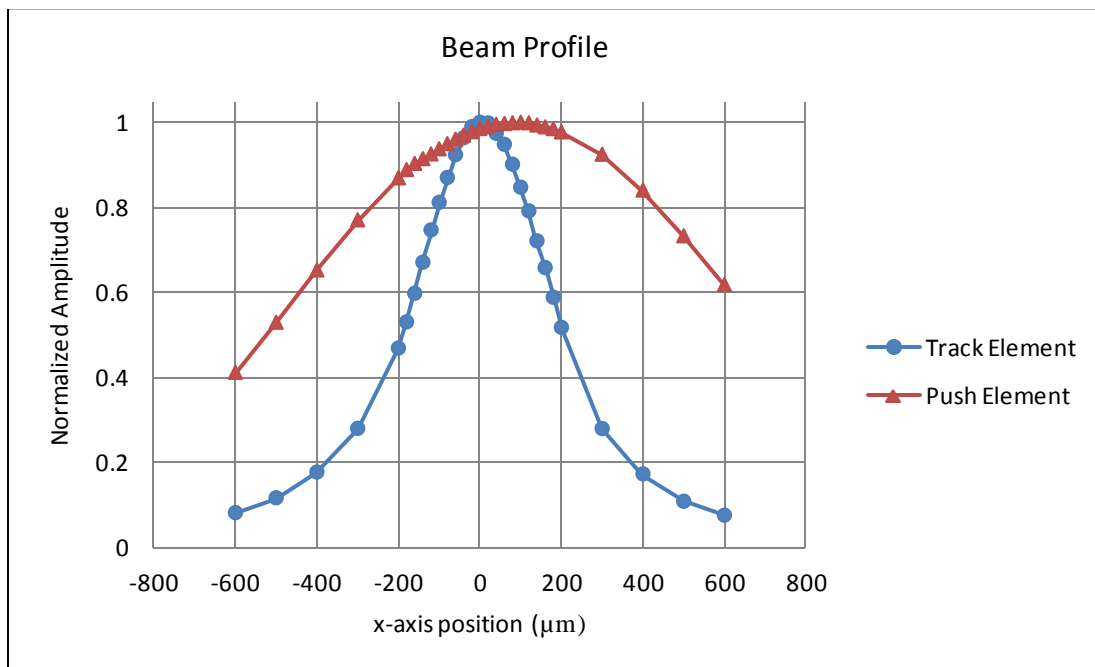
Figure 3.1: Transverse profile of dual element transducer. The focal points of the two elements are shifted by roughly 100 μm.
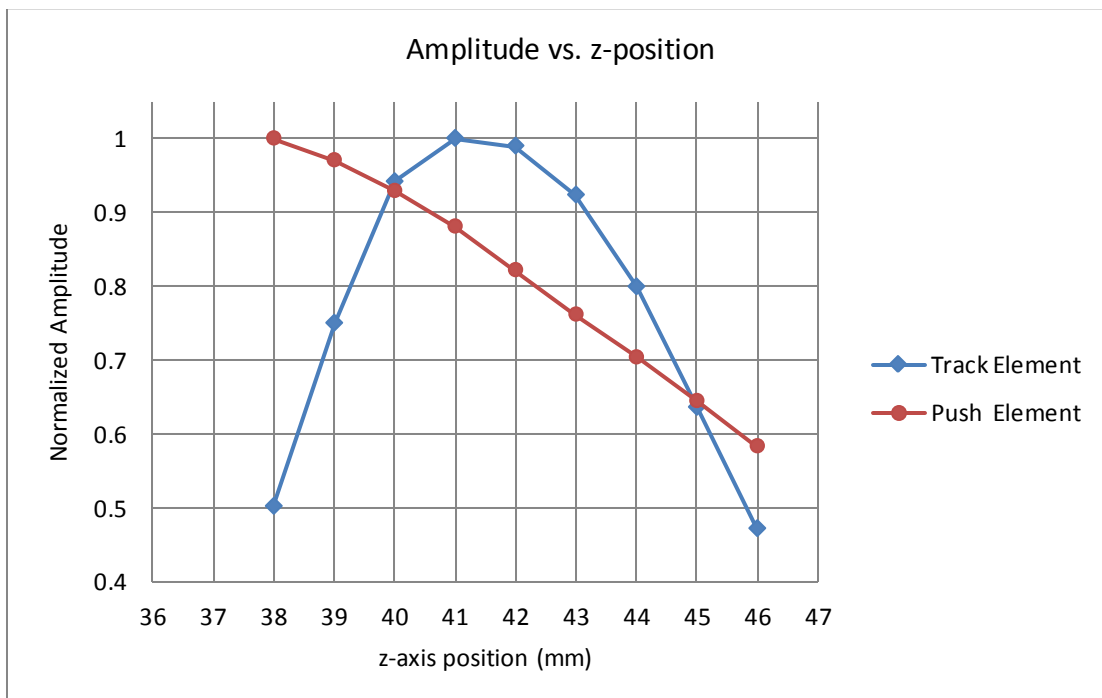
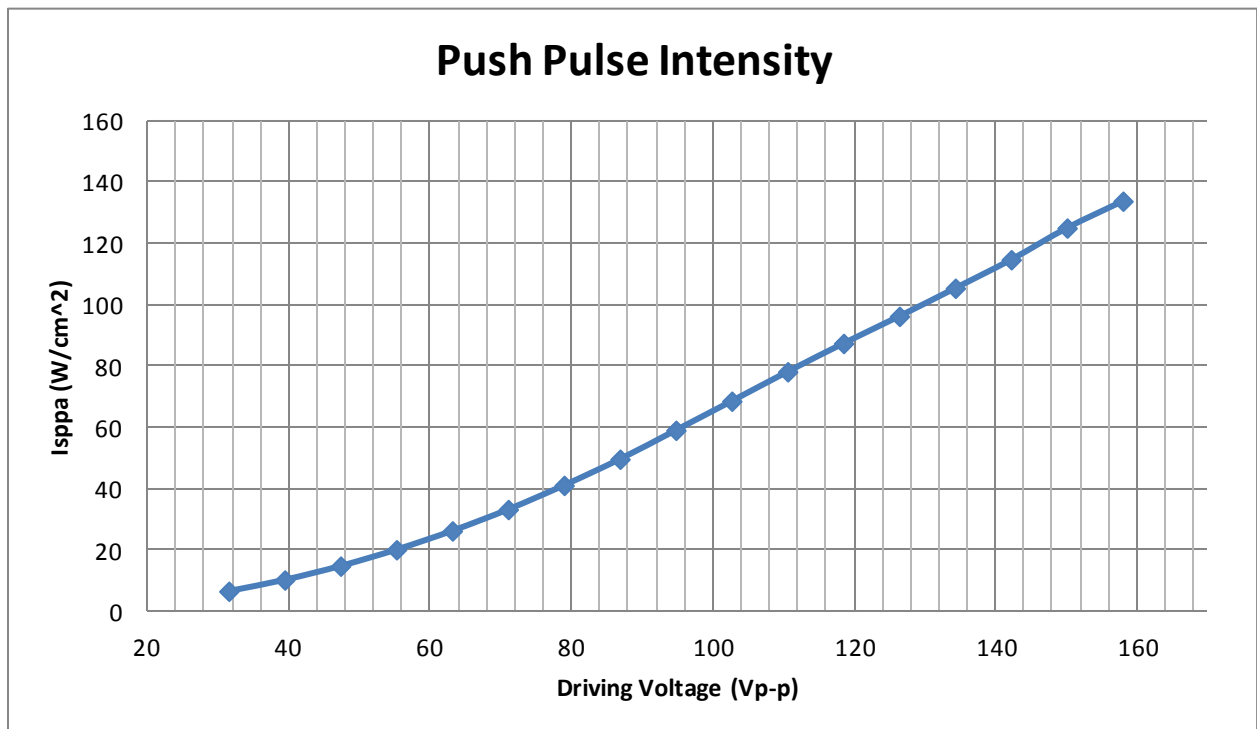Figure 3.2: Axial profile of both elements of the transducer in the vicinity of the focal plane at 41 mm.

Figure 3.3: Spatial peak, pulse average intensity (I_{sppa}, W/cm^2) of the acoustic radiation force generating element. Measurements were taken at the focal point of the tracking element.

2.9mm, 150mV, 10MHz HPF

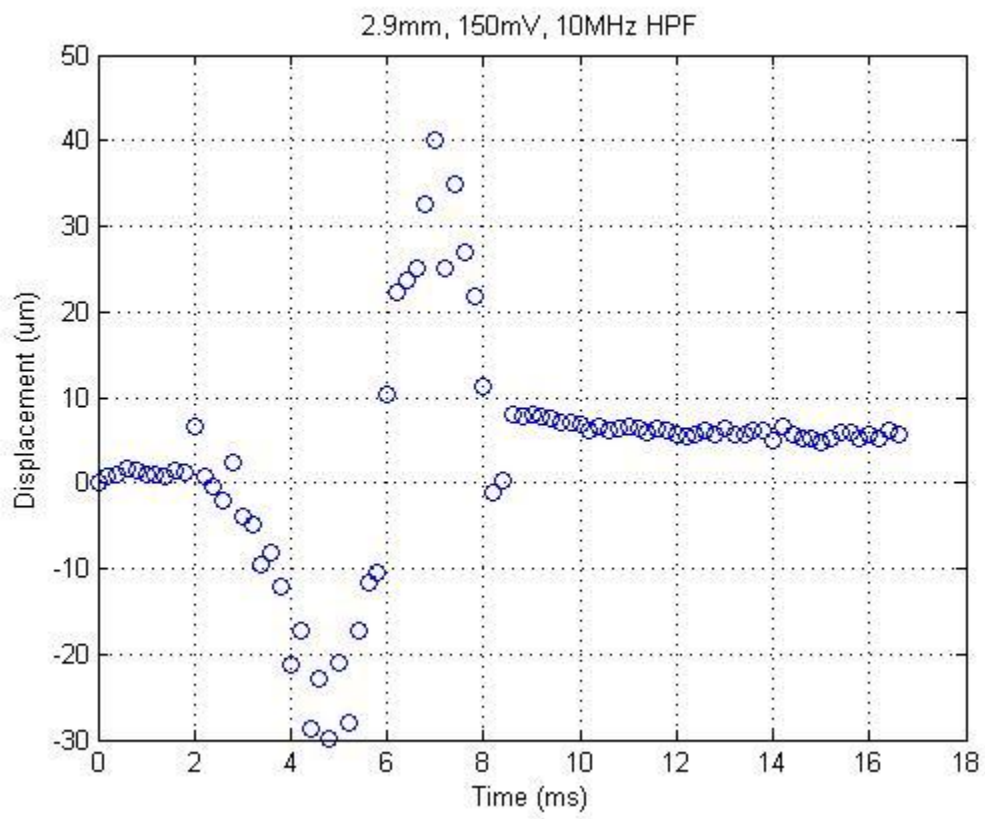Figure 3.4: Bubble oscillating first in the direction of the acoustic radiation and then reversing and moving in the direction opposite to the direction of the acoustic radiation and towards the transducer. Measurement was performed in a gelatin phantom.
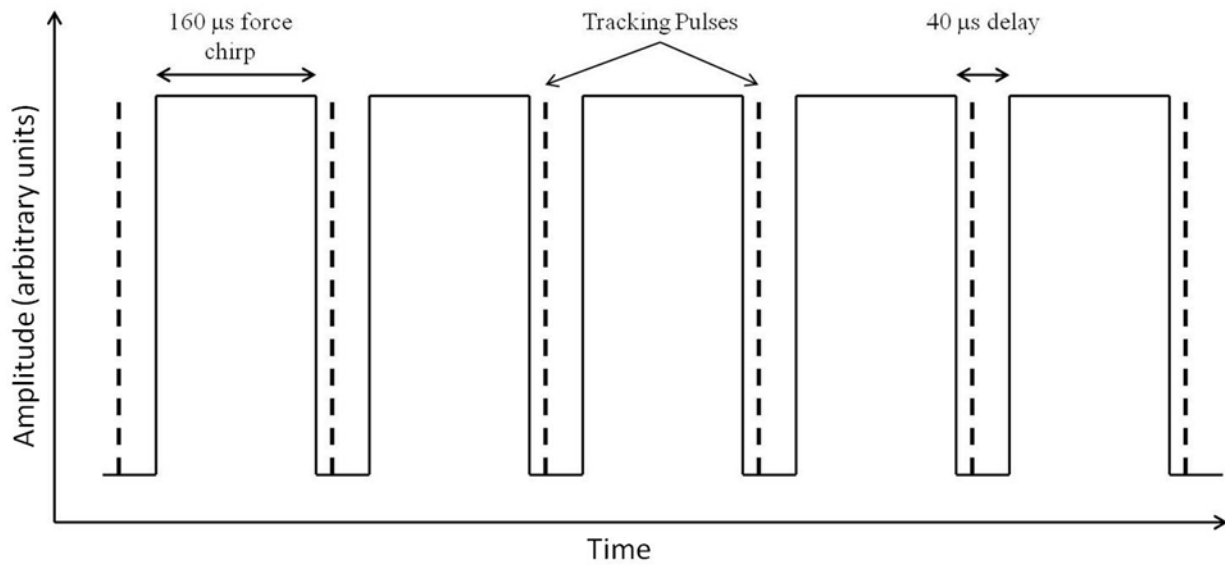
Figure 3.5: Notched force chirp pulse. The force chirp contains 40 µs notches with the imaging

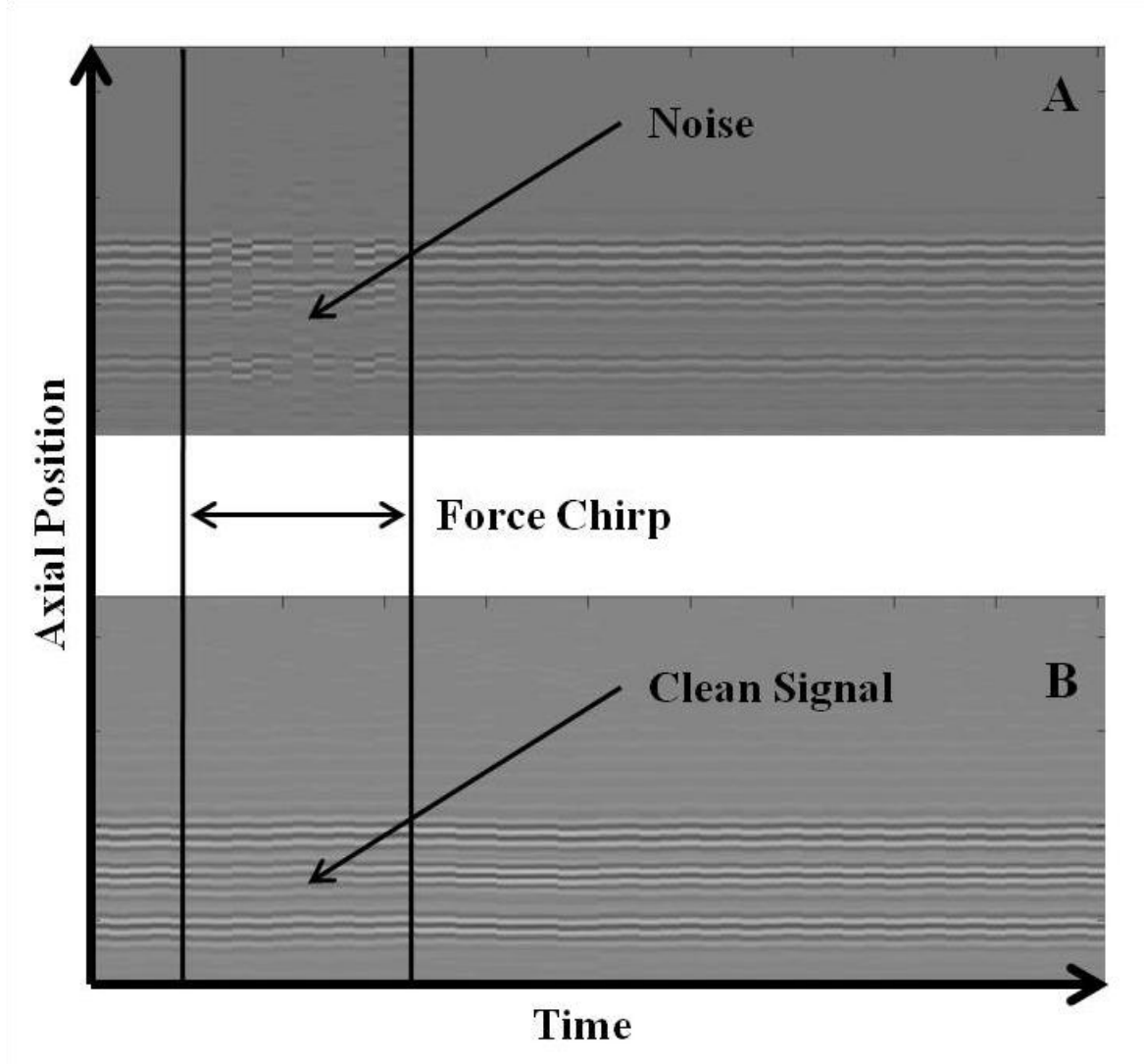pulse echoes hidden within them. This reduces noise in the A-scan signal.

Figure 3.6: Demonstration of the effect of the notched force chirp pulse on noise in the A-scan.

The noise artifacts in panel B are completely removed when compared to panel A.

3.7 References

AIUM/NEMA: Acoustic Output Measurement Standard for Diagnostic Ultrasound Equipment. Revision 3. Nema Standards Publication UD 2-2004. American Institute of Ultrasound in Medicine. Laurel, MD. National Electrical Manufactures Associaton. Rosslyn, VA. 2004.

Erpelding, T. N., Hollman, K. W., & O'Donnell, M. (2007). Bubble-based acoustic radiation force using chirp insonation to reduce standing wave effects. *Ultrasound in medicine & biology*, *33*(2), 263-269.

Tang S, and Gregory T. Clement. Standing Wave Suppression for Transcranial Ultrasound by Random-Modulation. IEEE Trans Biomed Eng. 2010 January; 57(1): 203–205. McCarey, B. E., Edelhauser, H. F. & Van Horn, D. L. (1973)

CHAPTER 4

Mapping Corneal Elasticity in the Cadaver Human Cornea

4.1 Introduction

The biomechanical properties of the cornea, along with the underlying corneal microstructure help determine the shape of the corneal surface, and thus also determine visual acuity. Since the cornea is a complex and inhomogeneous structure, it is expected that the elastic properties of the tissue will vary throughout its volume both axially and peripherally.

Numerous methods have been used to evaluate corneal elasticity, including strip testing, globe inflation, atomic force microscopy, and various ultrasonic methods. Earlier methods, such as globe inflation and strip testing treated the cornea as a homogenous material, measuring a bulk material property and not localized elastic moduli [Nyquist 1968, Hoeltzel et al. 1992, Zeng et al. 2001, Woo et al. 1972, Jue and Maurice 1986, Shin et al. 1997, Hjortdal 1995, Hjortdal 1996]. The elastic properties as they varied throughout the cornea were not addressed. However, the cornea is a complex, non-homogenous tissue composed of different layers and varying microstructure radially. There is significant interweaving of stromal lamellae in the anterior cornea, while this interweaving is absent in the posterior [Komai and Ushiki 1991, Radner et al. 1998, Radner et al. 2002, Jester et al. 2010]. Additionally, the interweaving in the anterior cornea affects the biomechanical properties. Interlamellar cohesive strength increases with lamellar interweaving. [Smolek and McCarey 1990, Smolek 1993]. Recently, atomic force microscopy was used to probe varying biomechanical properties through the thickness of the cornea [Last et al. 2012]. It was found that Bowman's layer was nearly three times stiffer than the anterior stroma. Similarly, the transverse shear modulus in the anterior cornea was found to be

significantly higher than central and posterior layers using torsional rheometry [Petsche et al. 2012]. A study using needle indentation found that the elastic modulus in the anterior cornea was nearly twice that of the posterior [Winkler et al. 2011 and Winkler et al. 2013]. Furthermore, this same study also revealed that collagen fiber branching-point density was four times higher in the anterior third of the cornea than in the posterior third. These studies have all shown that there is some depth dependence in corneal elasticity. As the cornea approaches the limbus and transitions into sclera tissue there is also a transition in the microstructure of the tissue. Furthermore, X-ray scattering data suggests that collagen fibril orientation shifts from a preferred orthogonal orientation in the central cornea to a preferred circumferential orientation near the limbus [Meek 2009]. The non-homogenous structure of the cornea, both through its thickness and radially towards the sclera, suggests that the elastic modulus will vary throughout the cornea. To date, there is still no consensus on regional corneal elastic modulus distribution, especially in the radial direction.

Recently, acoustic radiation force elastic microscopy (ARFEM) was used to measure localized elastic moduli in the human cornea [Mikula 2014]. Acoustic radiation force elastic microscopy (ARFEM) uses a low frequency, high intensity acoustic force to displace a femtosecond laser generated microbubble within the cornea, while using a high frequency, low intensity ultrasound to track the position of the microbubble within the tissue [Erpelding et al. 2005]. The elasticity measurement is localized to the exact position of the microbubble, which can be created at any position within the cornea. This feature makes ARFEM ideal for probing biomechanical properties throughout the cornea. In this chapter, ARFEM was used to measure elasticity at varying positions throughout the cornea, with the goal of creating a map of corneal elastic moduli.

4.2 Methods

4.2.1 ARFEM Setup

The system is essentially comprised of three core components, a femtosecond laser, a dual element ultrasound transducer, and a sample chamber. The laser is a commercial Ti:sapphire femtosecond laser (Coherent Inc., Santa Clara, CA) and produces 130 fs pulses at a wavelength of 800 nm. The ultrasound transducer has two elements, an outer low frequency, high intensity force generating element, and in an inner low intensity, high frequency tracking, or A-scan element. The outer force generating, or pushing, element has a central frequency of 1.7 MHz and a spatial peak, pulse average intensity (I_{sppa}) of 125 Watts/cm^2. The inner A-scan element has a central frequency of 17 MHz. The elements are confocal and both have a focal length of 41 mm. The A-scan element is driven by a commercial pulser-receiver (Panametrics Model 5072PR, Waltham, MA) at a pulse repetition frequency of 5 kHz. The pushing element is driven by an arbitrary function generator (Agilent Technologies Model 3314a, Palo Alto, CA) feeding into a 50 dB amplifier (ENI Model 240L, MKS Instruments, Wilmingtom, MA).

The corneal sample is embedded in gelatin within the sample chamber, while the rest of the chamber is filled with degassed, distilled water for acoustic coupling. The chamber itself is mounted to a 3-D microstage, allowing for the placement of the microbubble anywhere within the cornea. The laser is focused through a 0.3 NA objective using 80 μJ pulse energy, creating a microbubble with a diameter of 22 ± 2 μm within the cornea. The bubble diameter was measured using a microscope. Once the bubble has been created, the outer element of the ultrasound

transducer generates an acoustic radiation force chirp with a duration of 2 ms. The bubble is displaced and tracked and related to the local elastic modulus.

4.2.2 Sample Preparation

Eight paired human cadaver eyes from four donors were obtained from the San Diego Eye Bank. The age of the 4 donors were 84 (female), 86 (male), 67(male), and 89 (female). The eyes were preserved within 24 hours of death and stored no longer than 5 days. Prior to the experiment, corneas were thinned to a physiological thickness of 500-570 μm by inflating the intact globe with 20% Dextran solution at 20 mmHg IOP. Central corneal thickness was monitored using a Reichert IOPAC pachymeter (Reichert, Depew, NY). The cornea was then excised, leaving a 2 mm scleral rim, and embedded in a 7.5% gelatin gel within the sample chamber. Experiments were only performed when the corneal thickness was in the physiological 500 to 570 μm range.

4.2.3 Elasticity Mapping

ARFEM measurements were taken in the central cornea (0 mm), at 2.5 mm (mid), and at 5 mm (peripheral) toward the limbus. At each of these locations, both the anterior and posterior 150 microns of the cornea were evaluated. At least five measurements were made in the immediate vicinity of each location. Figure 4.1 shows the location of the measurements within the cornea and the orientation of the cornea on the surface of the gel. The cornea was placed on the gelatin surface in such a way that half of the cornea was flat against the gelatin surface, with the other half curving upward. Additional gelatin was then poured on top of the sample and allowed to harden in the refrigerator. This was necessary due to the fact that the anterior corneal surface must be perpendicular to the laser beam for optimal bubble creation. Additionally, we

seek to measure the elastic modulus in the direction perpendicular to the surface of the cornea. To that end, the incident acoustic radiation force must be normal to the cornea surface. Laying the half cornea flat against the gel allowed measurements to be made both in the central and peripheral regions without having to reorient the cornea, which would require pouring new gel and subjecting the cornea to new hydration conditions with respect to the previous measurement. During the measurements, the cornea was oriented so that the acoustic force and resultant microbubble displacements were perpendicular to the corneal surface; therefore the experiment measured corneal elasticity in the direction perpendicular to the corneal surface.

4.3 Results

The elastic modulus in the direction perpendicular to the corneal surface (normal) was found to vary with location in the cornea. In the anterior cornea, the mean elastic moduli were 4.2 ± 1.2kPa, 3.4 ± 0.7 kPa, and 1.9 ± 0.7 kPa in the central, mid, and peripheral regions respectively. These results are summarized in Figure 4.2. In the posterior cornea, the mean elastic moduli were 2.3 ± 0.7 kPa, 1.6 ± 0.3 kPa, and 2.9 ± 1.2 kPa in central, mid, and peripheral regions respectively. These results are summarized in Figure 4.3. While the anterior cornea was roughly twice as stiff as the posterior cornea in the central and mid cornea, the trend shifted toward the periphery with the anterior elastic modulus decreasing with respect to the posterior. A direct comparison of the anterior and posterior cornea is presented in Figure 4.4.

4.4 Discussion

The ARFEM technique used in this study has the significant limitation of being unable to measure the elasticity distribution in the mechanically loaded cornea and intact globe. Given the nature of the current ARFEM device, the cornea must be excised from the globe and placed between the laser objective and ultrasound. Additionally, the cornea is laid flat against the gelatin surface in such a way that half of the cornea curves unnaturally upward. The mechanical effect of this curvature is assumed to be negligible. Previous measurements in the central cornea with the natural radius of curvature preserved showed the same 2:1 ratio is elasticity between the anterior and posterior regions [Mikula 2014].

With these limitations, this study found the elasticity in the central anterior cornea to be nearly twice the elasticity in the central posterior cornea. Similar results were found using needle indentation which revealed the same 2 to 1 ratio in elastic modulus between the anterior and posterior central cornea [Winkler et al. 2011]. Likewise, the mid anterior cornea was found to be twice as stiff as the mid posterior cornea. Structurally, the anterior cornea possesses highly interwoven collagen structure compared to the relative homogeneity in the posterior. Despite this apparent correlation between microstructure and elasticity in the central and mid-cornea, the trend was not observed in the peripheral cornea. The peripheral anterior cornea was found to be roughly half as stiff as the central anterior, while the peripheral posterior cornea was found to be roughly 30 percent stiffer than the central posterior cornea. It is interesting to note that interlamellar cohesive strength in the stroma is twice as strong in the periphery as it is centrally [Smolek et al. 1990]. Though ARFEM does not measure interlamellar cohesive strength, both results suggest a biomechanical change in the peripheral cornea. Furthermore, the peripheral anterior corneal elasticity is roughly 2/3 that of the peripheral posterior cornea. It appears as

though in the periphery, the anterior and posterior corneas nearly reverse elastic moduli relative to one another. However, anterior collagen interweaving does not differ significantly between the central and peripheral cornea [Winkler 2013]. Using non-linear optical high resolution macroscopy (NLO HRMac), collagen fiber angle distribution relative to the corneal surface was imaged radially along the cornea. The collagen angle relative to the surface was used as a metric for collagen interweaving. They found no statistical difference in collagen angles between the central and peripheral cornea. Figure 4.5 shows a typical image of the human cornea using this technique. The wrinkles on the posterior surface in panel A are artifacts from the mounting of the sample. Panels B, C, and D show that the anterior interweaving relative to posterior collagen orientation is preserved from the center to the periphery. However, structural differences in the periphery of the cornea maybe masked by the shifting orientation of lamellae from central to peripheral. Structurally, the cornea is changing as it nears the limbus, with collagen fibers adopting a more tangential (circumferential) orientation in the periphery, as imaged by wide angle x-ray scattering [Meek 2011]. Collagen fibers in this orientation would not have been detected in the previous work by Winkler et al., as HRMac does not image en face collagen fibers. The effect of potential tangential oriented collagen fibers on local elasticity is unknown. As the lamellae exit the cornea and change in orientation they transition into the structurally unique sclera. The biomechanical effects of the insertion of collagen lamellae into the sclera are unknown. Furthermore, the periphery may be subject to different swelling conditions because the peripheral edge of the sample is exposed directly to the gelatin medium. The cornea is indeed thicker in the periphery and hydration differences between the anterior and posterior could be exacerbated to the proximity of the measurements to the edge of the sample.

In addition to collagen microstructure, proteoglycan (PG) distribution throughout the cornea may also have an effect on local elasticity as measured by ARFEM. Specifically, it is pertinent to explore any differences in PG distribution between the anterior and posterior cornea, both centrally and peripherally. A proteoglycan (PG) consists of a core protein with one or more covalently attached glucosaminoglycans (GAG). The GAG is highly polar, negatively charged, and as such binds water. The concentration of keratan sulfate, the most prominent PG in the cornea, increases from anterior to posterior in the central cornea [Davies 1997]. Furthemore, stromal swelling is almost entirely caused by the gel pressure (swelling pressure) generated by negatively charged proteoglycans [Hodson 1997]. When these findings are considered along with the highly interwoven structure of the anterior cornea, it seems reasonable that the anterior cornea is resistant to edema when compared to the posterior cornea [Muller 2001, Meek 2003]. Peripherally, our results show that the anterior corneal elasticity is roughly half that of the central anterior cornea. With studies showing that *en face* collagen interweaving does not change between the center and periphery, this result is particularly interesting. As with the central cornea, it would be interesting to know the trend in PG distribution in the peripheral cornea. It is possible that local PG concentration and the resultant swelling pressure have an effect on local elasticity as measured by ARFEM. Unfortunately, the literature does not reveal many telling details about the differences in PG concentration between the central and peripheral cornea. One study looked at total soluble protein concentration between the anterior and posterior cornea, traversing across the cornea from the limbus to the central cornea. They found that total soluble protein concentration in the peripheral anterior cornea was nearly twice that of the central anterior cornea [Gong 1997]. Though it may appear that this result corroborates our findings between central and peripheral elasticity, the correlation could be entirely coincidental since they

were not specifically measuring PG distribution. To truly resolve this issue, a specific measurement of the axial PG gradient in the peripheral cornea would need to be performed. Such a gradient in PG concentration could affect local hydration, thus affecting elasticity.

4.5 Conclusion

This study found that there is a unique distribution of elasticity both axially and radially throughout the cornea. While ARFEM results in the central cornea are in reasonable agreement with other techniques including needle indentation and torsional rheometry, lack of mechanical data in the peripheral cornea make comparisons difficult. It is however clear that the full picture of corneal biomechanics is quite broad, involving complex and inhomogenous collagen microstructure to varying concentration of proteoglycans throughout the cornea. A better understanding of these variables along with elasticity measurements, especially in the peripheral cornea, would certainly help in completing the picture.
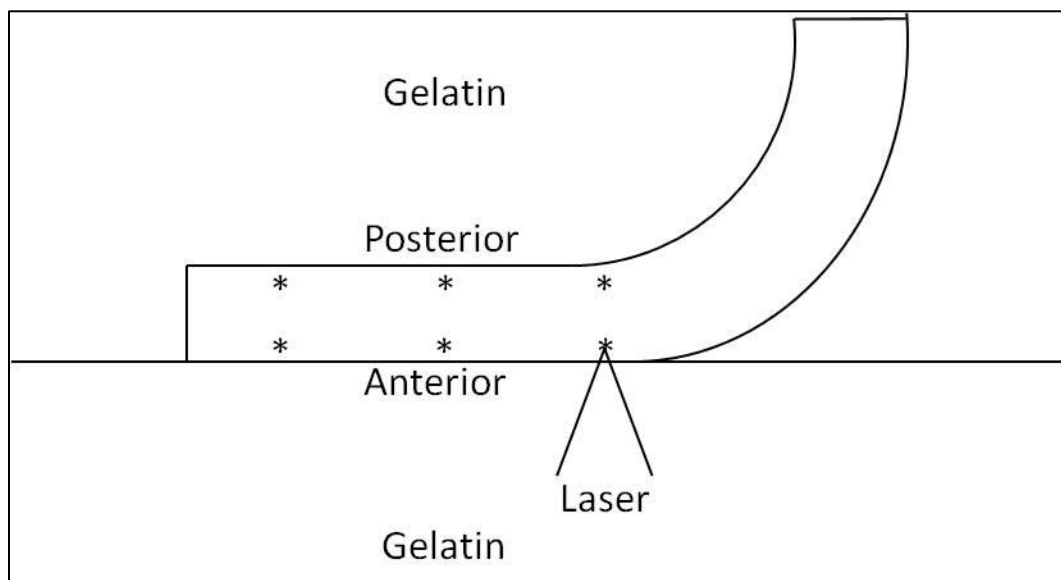
Figure 4.1: Corneal orientation and ARFEM measurement locations. The sample is flattened against the surface of the gel so that measurements can be made at multiple locations without having to reposition the cornea.
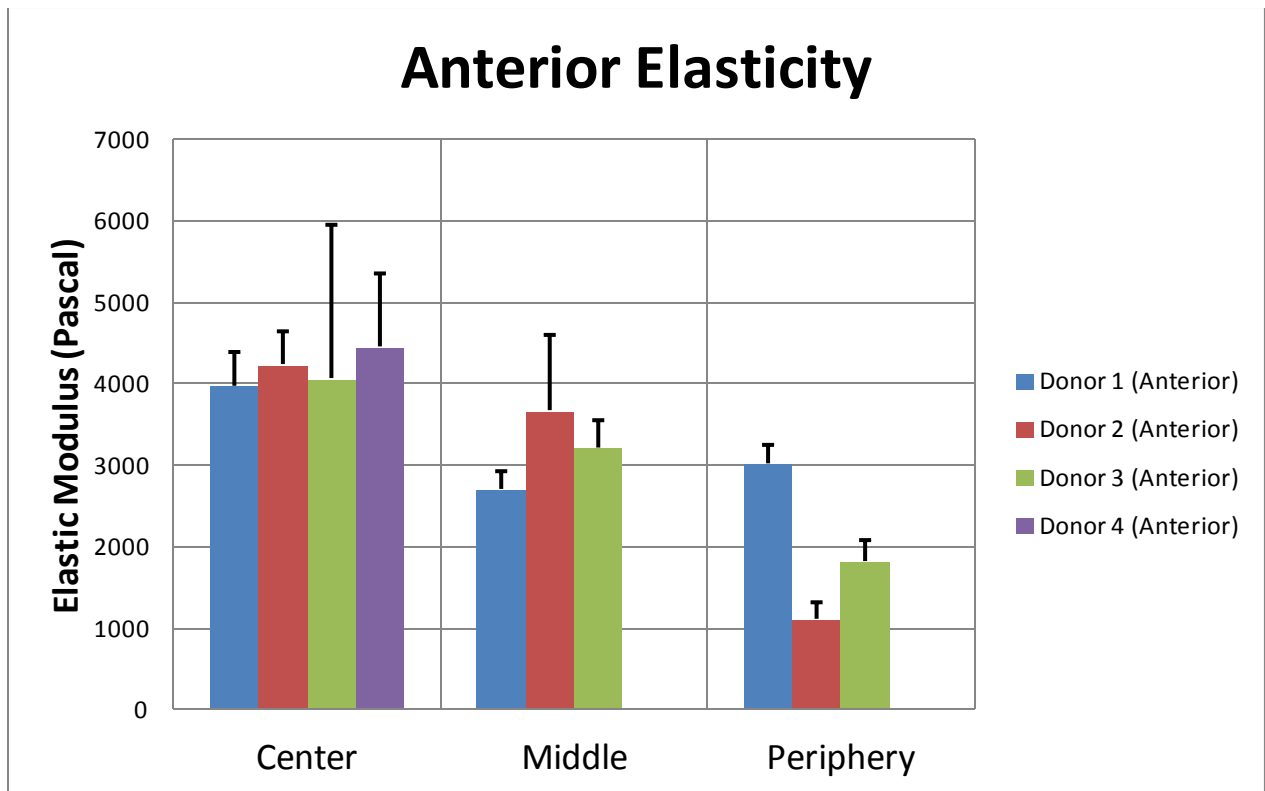
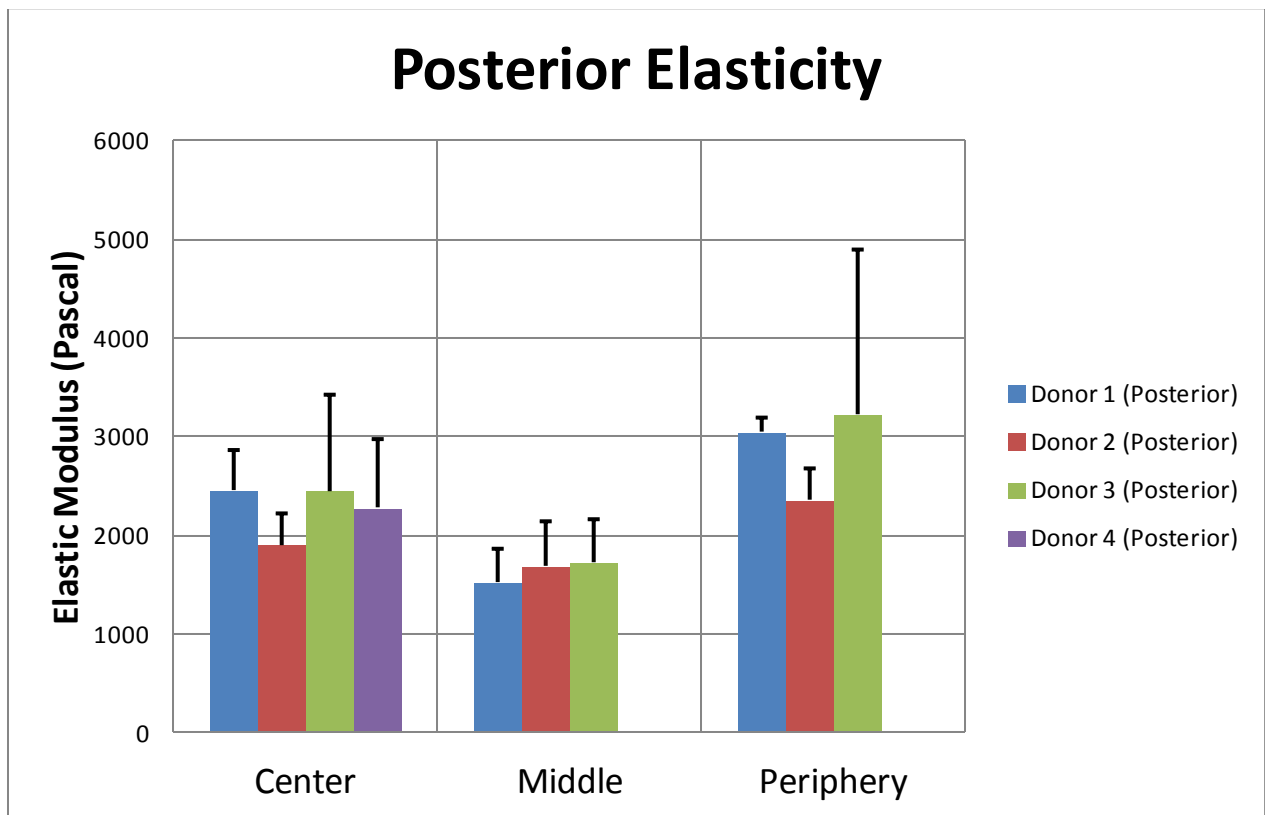Figure 4.2: Normal elastic modulus in the anterior 150 μm of cornea from the center to the periphery.

Figure 4.4: Normal elastic modulus in the posterior 150 μm of cornea from the center to the periphery.
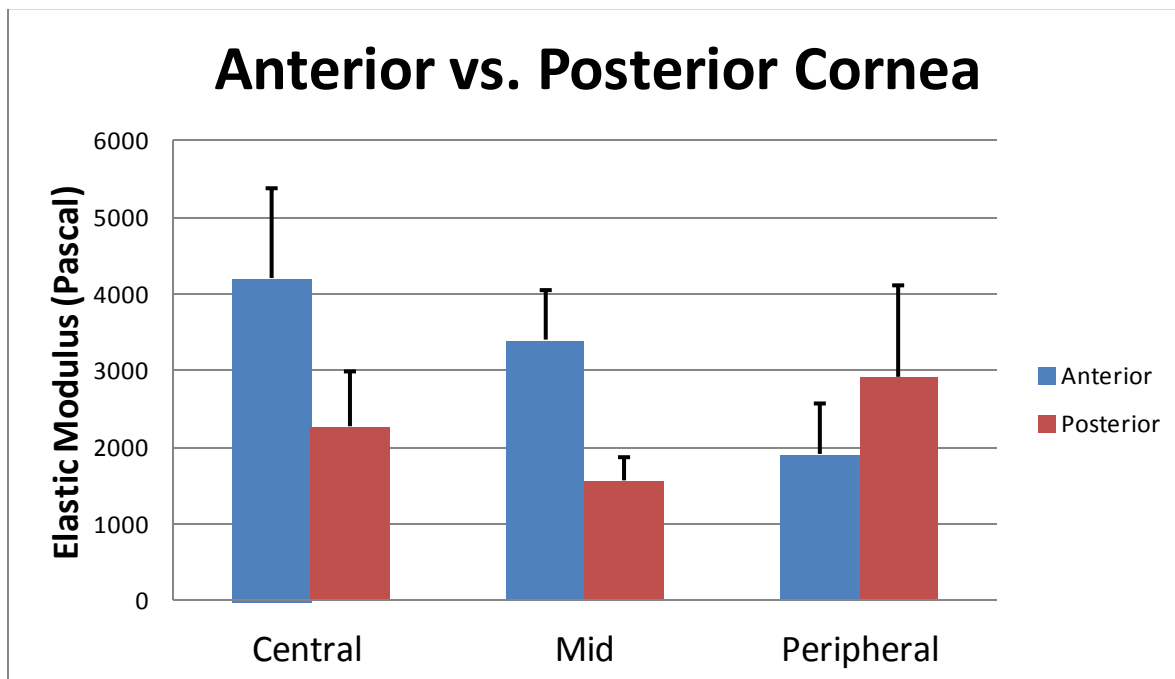
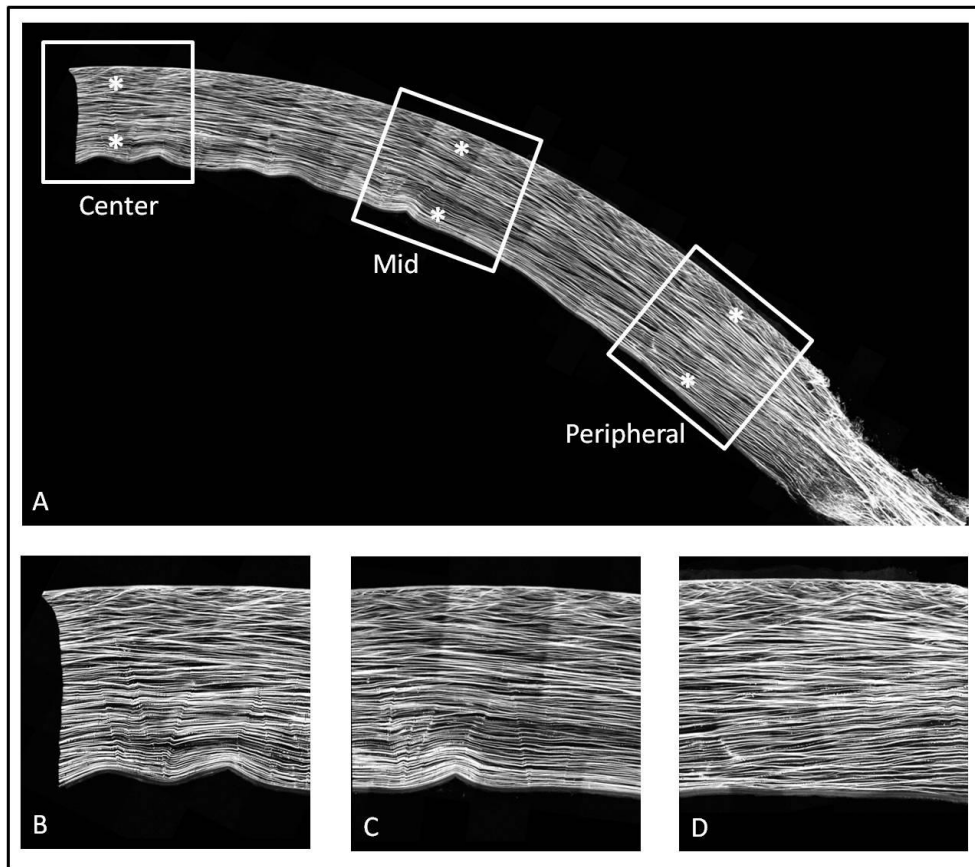Figure 4.4. The mean elastic moduli for 8 corneal samples.

Figure 4.5. HRMac images of collagen structure in the cornea. Panel A shows half of a human cornea from the center to the limbus. While the posterior lamellae continue uninterrupted into the sclera, the anterior interwoven region seems to end abruptly at the limbus. Panels B, C, and D show the center, middle, and peripheral measurement locations, respectively.

4.5 References

Bryant M, McDonnell p. Constitutive Laws for Biomechanical Modeling of Refractive Surgery. J. Biomech. Eng. 118, 473. 1996.

Davies, Y., Fullwood, N. J., Marcyniuk, B., Bonshek, R., Tullo, A., & Nieduszynski, I. A. (1997). Keratan sulphate in the trabecular meshwork and cornea. Current eye research, 16(7), 677-686.

Erpelding T, Hollman K, O'Donnel M. "Bubble-based acoustic radiation force elasticity imaging." IEEE Trans Ultrason Ferroelectr Freq Control. 52:971-979. 2005.

Gong, H., Johnson, M., Ye, W., D Kamm, Roger., & Freddo, T. F. "The non-uniform distribution of albumin in human and bovine cornea." Experimental eye research, 65(6), 747-756. (1997).

Hjortdal J O. Extensibility of the normo-hydrated human cornea. Acta ophthalmologica Scandinavica. 73. 12-17, 1995.

Hjortdal J O. Regional elastic performance of the human cornea. J. Biomechanics, 1996. 29:931-942.

Hodson, S. A. (1997). Corneal stromal swelling. Progress in Retinal and Eye Research, 16(1), 99-116

Muller L, Elisabeth Pels, Gijs F J M Vrensen. The specific architecture of the anterior stroma accounts for maintenance of corneal curvature. Br J Ophthalmol 2001;85:437-443

Hoeltzel DA, Buzard K, Altman P. Experimental determination and comparison of the mechanical response of bovine and rabbit corneas as a model for predicting the mechanical behavior of the human cornea. J. Biomech. Eng. 1992, 114:202-215.

Jue B, Maurice D. The mechanical properties of the rabbit and human cornea, Journal of Biomechanics, Volume 19, Issue 10, 1986, Pages 847-853.

Last JA, Thomasy SM, Croasdale CR, Russell P, Murphy CJ. "Compliance profile of the human cornea as measured by atomic force microscopy." Micron. 43(12):1293-8. 2012.

Meek KM, Boote C. "The use of X-ray scattering techniques to quantify the orientation and distribution of collagen in the corneal stroma." Prog Retin Eye Res. 28(5):369-92. 2009.

Mikula, E., Hollman, K., Chai, D., Jester, J. V., & Juhasz, T. (2014). Measurement of Corneal Elasticity with an Acoustic Radiation Force Elasticity Microscope. Ultrasound in medicine & biology, 40(7), 1671-1679.

M K Smolek, B E McCarey .Interlamellar adhesive strength in human eyebank corneas. IOVS June 1990 31:1087-1095.

Nyquist G, Rheology of the cornea: Experimental techniques and results, Experimental Eye Research, Volume 7, Issue 2, April 1968, Pages 183-188.

Petsche SJ, Chernyak D, Martiz J, Levenston ME, Pinsky PM. "Depth-dependent transverse shear properties of the human corneal stroma." Invest Ophthalmol Vis Sci. 2012 Feb 21;53(2):873-80. 2012.

Radner W, Mallinger R. Interlacing of collagen lamellae in the midstroma of the human cornea. Cornea. 2002. 21:6:598-601.

Radner W, Zehetmayer M, Aufreiter R, Mallinger R. Interlacing and cross-angle distribution of collagen lamellae in the human cornea. Cornea. 1998. 17:5:537-543.

S. L-Y Woo, A. S. Kobayashi, W. A. Schlegel, C. Lawrence, Nonlinear material properties of intact cornea and sclera, Experimental Eye Research, Volume 14, Issue 1, July 1972, pg. 29-39

Shin T, Vito R, Johnson L, Bernard E. McCarey. The distribution of strain in the human cornea. Journal of biomechanics 1 May 1997 (volume 30 issue 5 Pages 497-503)

Smolek MK. Interlamellar cohesive strength in the vertical meridian of human eye bank corneas. IOVS September 1993 34:2962-2969.

Winkler, M., Shoa, G., Xie, Y., Petsche, S. J., Pinsky, P. M., Juhasz, T., ... & Jester, J. V. (2013). Three-dimensional distribution of transverse collagen fibers in the anterior human corneal stroma. Investigative ophthalmology & visual science, 54(12), 7293-7301.

Winkler M1, Chai D, Kriling S, Nien CJ, Brown DJ, Jester B, Juhasz T, Jester JV. "Nonlinear optical macroscopic assessment of 3-D corneal collagen organization and axial biomechanics." Invest Ophthalmol Vis Sci. 11;52(12):8818-27. 2011.

Y Komai, T Ushiki. The three-dimensional organization of collagen fibrils in the human cornea and sclera. IOVS July 1991 32:2244-2258.

Zeng Y, Yang J, Huang K. A comparison of biomechanical properties between human and porcine cornea. J Biomech. 2001, 34:533-537.

CHAPTER 5

ARFEM Applications: Keratoconus and Corneal Crosslinking

5.1 Introduction

Keratoconus is a disorder characterized by a thinning of the cornea and weakening of the stroma. This gives rise to an outward protrusion of the cornea into a conical configuration. The resulting astigmatism and myopia have a dramatic negative effect on visual acuity, often necessitating a corneal transplant [Bron 1988; Bron & Rabinowitz 1996; Rabinowitz et al. 1998; Sherwin & Brookes 2004). While there is no consensus on the prevalence of keratoconus, estimates are in the range of 1 in 2000 [Rabinowitz 1998, Patel and Vellara 2015]. Numerous structure differences are thought to be associated with keratoconus (KC) in addition to the characteristic thinning of the stroma. It was observed that the number of lamellae is reduced in the KC cornea but that the thickness of lamellae is unlaltered [Takahashi et al. 1990]. In severe KC, stromal scarring manifests while the basement membrane greatly thickens and collagen fibril spacing is reduced in all layers [Akhatar et al. 2008]. Another interesting structural difference in the KC cornea is the absence of the inferior-superior and nasal-temporal preferred lamellar collagen orientation when compared to a normal cornea. Additionally, some lamellae even take a preferred tangential orientation around the edge of the protruding KC cone [Meek et al. 2005]. One proposed mechanism for the development of KC is so called 'slippage' between collagen fibrils. There is much resistance to surgical dissection of the stroma suggesting that there are some elements such as matrix proteoglycans that may bind the lamellae together. If this interfibrillar glue were to weaken then the collagen lamellae could possible tear apart and 'slip' past one another [Meek 2005]. A reduction in contact points between lamellae is analogous to less interweaving, which could potentially weaken the local structure. Additionally, this could

lead to an effective lengthening of the lamellae which would then be free to bow outward in response to the new found 'slack' being pushed on by IOP.

UVA corneal collagen crosslinking has emerged as a promising technique to treat keratoconus [Spoerl et al. 1998, Wollensack et al. 1998]. In this method the affected cornea is soaked in Riboflavin (photosensitizer) and then irradiated with UV-A light. The riboflavin is a strong absorber of UV light, which after it is activated, produces radicals that interact with corneal proteins leading to covalent bonding within collagen fibrils, much in the same way as photopolymerization in polymers [Kamaev et al. 2012]. The goal of the crosslinking is to increase or restore the mechanical strength of the stroma so that the cornea can better resist outward bowing and thinning. UVA- Riboflavin crosslinking regularly achieves an elastic modulus increase of between a factor of 2 and 4 [Kohlhaas et al. 2006, Seifert et al. 2014, Knox et al. 1995]. In this respect, UVA-riboflavin crosslinking is a very effective treatment for keratoconus. However the method is not without shortcomings. In addition to free radicals causing cell death, UVA-riboflavin crosslinking (CXL) is limitied to the anterior 300 μm of the cornea, though some researchers have reported no stiffening effects beyond the anterior 200 μm [Seifert et al 2014]. Recently, femtosecond lasers have seen increased use as a replacement for UVA light in the crosslinking procedure [Chai et al. 2013, Wollensack 2014]. Femtosecond laser light has the advantage of a precisely controllable and minute focal volume where CXL occurs with the advantage of added penetration depth. As opposed to UVA light which can be regarded as more of a shotgun approach in that the light used is a large diameter, collimated, and continuous, the femtosecond laser pulses can be finely tuned to crosslink anywhere within the cornea at micron resolution. Since this crosslinking process relies on the absorption of multiple photons at once, this method is referred to a non-linear optical crosslinking, or NLO CXL. In this

chapter pilot data are taken from 2 keratoconus corneas. Additionally, we evaluate UVA and NLO crosslinked rabbit corneas.

5.2 Methods

5.2.1 Control Rabbit Eyes

Rabbit eyes were shipped overnight on ice (Pel-Freez, Rogers, AK), rinsed in minimal essential medium (Invitrogen, Carlsbad, CA), and placed in 12-well tissue culture plates containing sufficient medium to cover the scleral portion of the globe, leaving the corneal surface exposed to air, to keep the corneal epithelium viable and maintain corneal transparency. The eyes were then placed in a humidified, CO_2 tissue culture incubator at 37°C for 1 hour, to allow corneal thickness to return to normal. Riboflavin was applied to the control corneas every two minutes for one hour [Chai et al. 2011].

5.2.2 UVA - Riboflavin CXL

The UVA riboflavin CXL cornea has riboflavin applied to its surface every two minutes for 30 minutes prior to UVA treatment. After 30 minutes, the cornea was irradiated for 30 minutes with a 3-mW/cm^2, 370-nm light source (PriaVision, Menlo Park, CA). Riboflavin was applied evey 2 minutes.

5.2.3 NLO CXL

A 760-nm FS laser beam was focused into the corneas through a 20×/0.75 NA objective lens (Zeiss). The corneas were tile scanned over a 5.2×5.2 mm area through the thickness of the

cornea at 2 μm axial steps using the MultiTime function in the LSM software. Each tile was raster scanned (512 lines) over a 455×455 μm area at 28 cm/s scan speed.

5.2.4 Keratoconus Corneas

3 keratoconus (KC) buttons were obtained from the Gavin Herbert Eye Insititute (UCI, Irvine, Ca) and were stored in Optisol no longer than 5 days after excision from the donor. ARFEM measurements were performed in the center of the buttons.

5.2.5 ARFEM Measurements

The rabbit corneas were excised from the globe, allowing a 1 mm sclera ring to remain. Both the KC and rabbit samples were mounted in the acoustic sample chamber and submerged in 7.5% gelatin. The samples were refrigerated to harden the gel. After the gel hardened the sample was allowed to return to room temperature before it was mounted to the ARFEM system. A femtosecond laser with a pulse length 130 fs, wavelength 800 nm, and pulse energy 8o μJ was used to created a microbubble in the sample corneas. A high intensity ultrasound with I_{sppa} 125 W/cm^2 displaced the bubble while tracking pulse echoes monitored its position. The maximum displacement is inversely proportional to local elastic modulus. The measurements measurements in the KC corneas were performed in the anterior and posterior central cornea. The measurements in the rabbit corneas were made in the anterior 150 μm of the corneas to ensure the crosslinked region was probed. At least 5 separate bubble were measure in the vicinity of the center of each cornea.

5.3 Results

The normal elastic moduli for the anterior KC corneas were 1456 ± 233 Pa, 1385 ± 510 Pa, and 2174 ± 324 Pa. The normal elastic moduli for the posterior KC corneas were 944 ± 192 Pa, 683 ± 255 Pa, and 1282 ± 626 Pa. The elastic moduli in the KC corneas were significantly lower than in normal cadaver human corneas. Figure 5.1 summarizes the anterior/posterior elasticity measurements in the 3 KC corneas. Figure 5.2 compares the average KC values with normal corneas.

The elastic moduli of the for control rabbit eyes were 600 ± 60 Pa, 610 ± 130 Pa, 640 ± 80 Pa, and 560 ± 140 Pa. The elastic modulus for the single UVA CXL treated eye was 1340 ± 190 Pa. The elastic moduli of the 3 NLO CXL treated corneas were 610 ± 110 Pa, 1060 ± 130 Pa, and 1060 ± 250 Pa. These results are summarized in Figure 5.3. The average elasticity of all controls was 610 ± 110 Pa.

5.4 Discussion

The pilot measurements in the KC corneas seem to indicate a softening/weakening in the KC cornea. Previous studies have indicated a loss of collagen lamellae in the KC cornea which could account for mechanical weakening [Takahashi 1990]. Furthermore, the loss of the preferred orthogonal orientation of lamellae indicated by Meek could also play some role in the weakening. Certainly more samples are needed to reach a conclusion. Compared with results obtained from normal human corneas, the KC corneas are roughly twice as soft.

With respect to crosslinking, both methods seemed successful in stiffening the rabbit eye. The NLO CXL procedure stiffened the cornea by 74%. Chai et al. were able to stiffen collagen

hydrogels by nearly 100% [Chai et al. 2013]. The UVA crosslinking was able to stiffen the cornea nearly a factor of 2.2.

5.5 Conclusion

ARFEM is an effective technique for validation the efficacy of crosslinking procedures. NLO CXL is a promising new technique that has the potential for highly customized and tuneable selective stiffening of the cornea. Due to its multiphoton action only in the focal volume, NLO CLX has a distinct advantage of traditional UVA CXL.
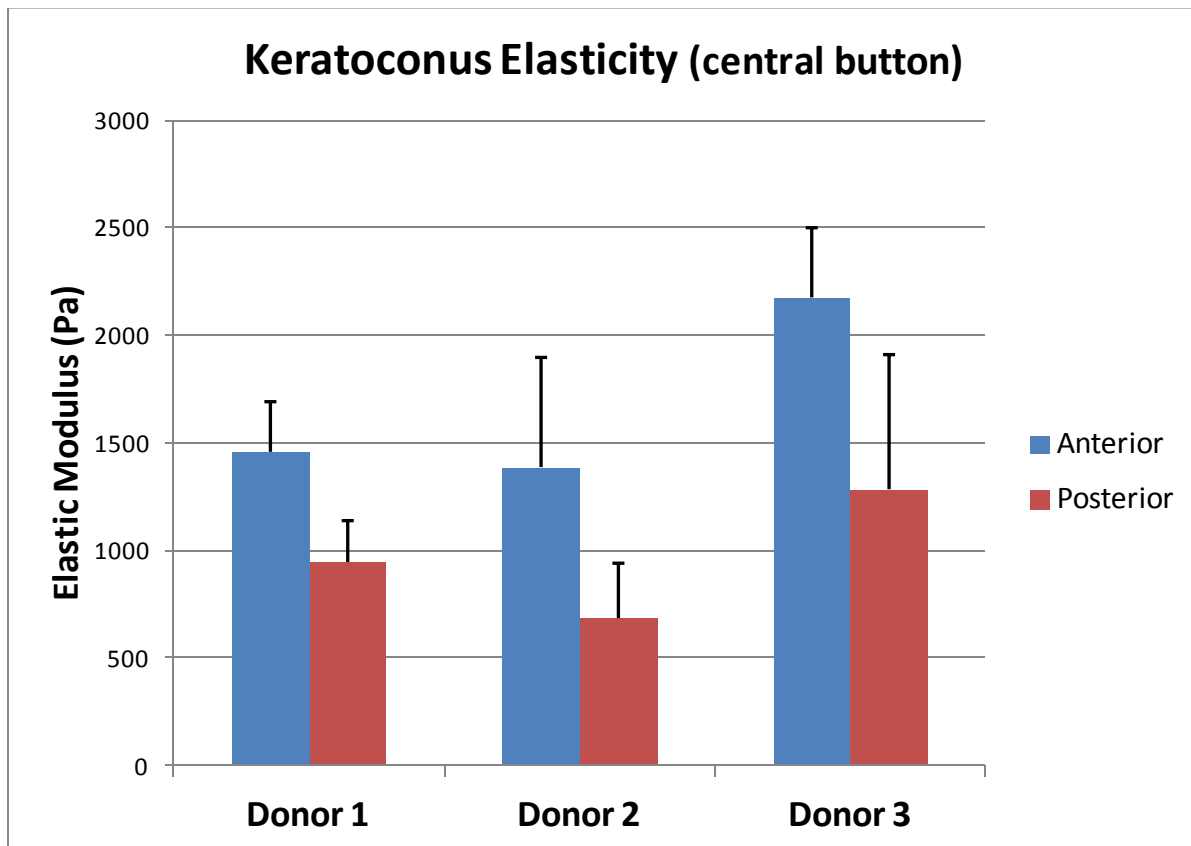
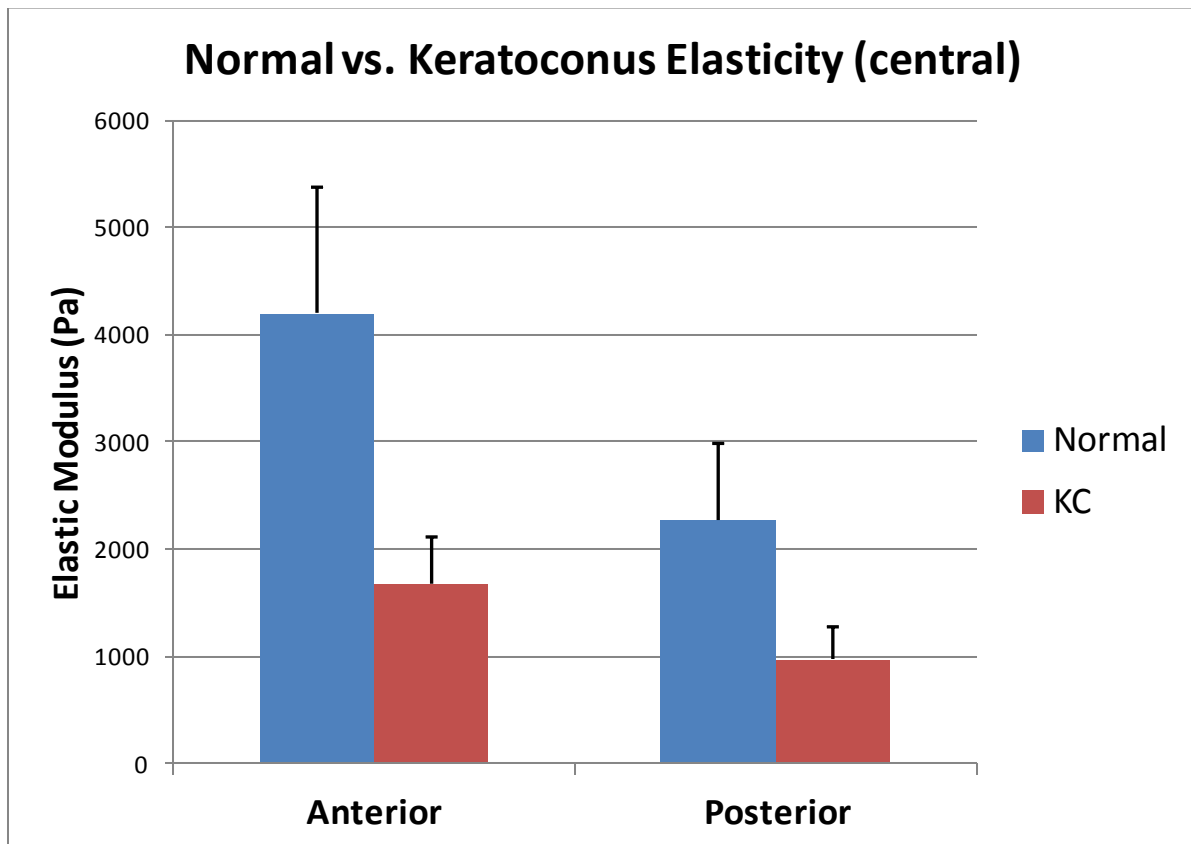Figure 5.1: ARFEM measurements in keratoconus buttons.

Figure 5.2: Normal human cadaver corneas vs. keratoconus corneas. All measurements were taken in the central cornea.
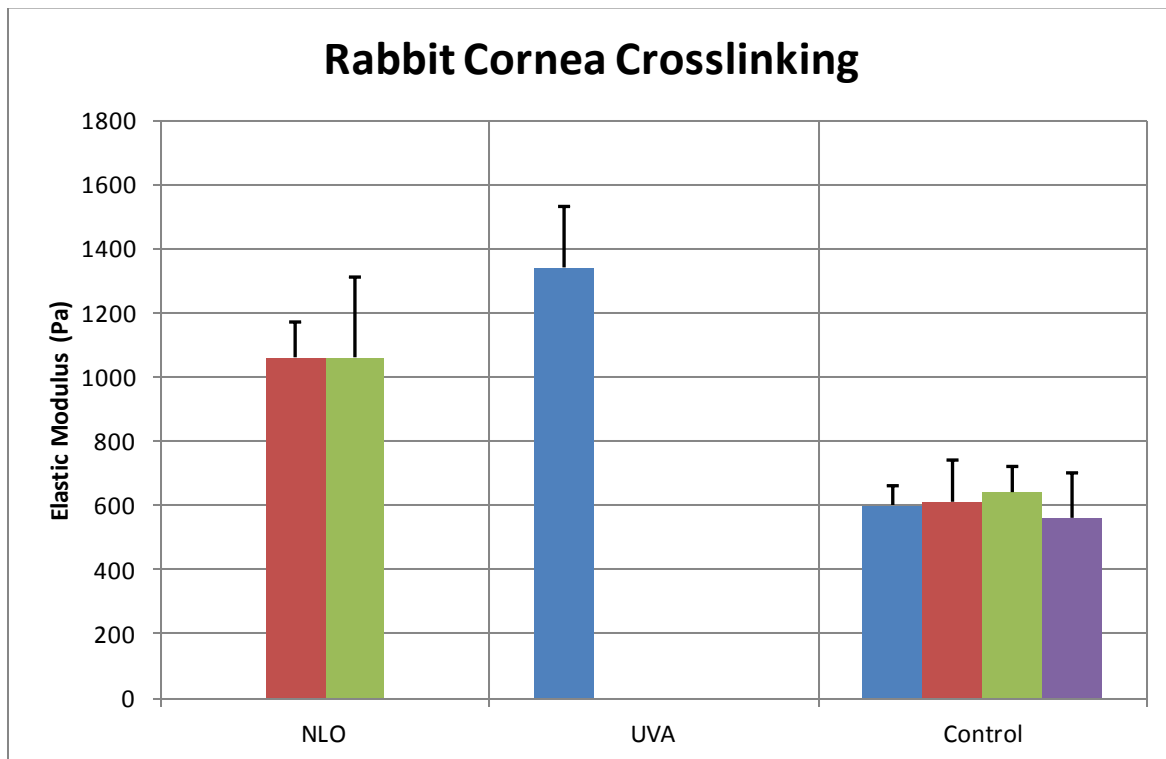
Figure 5.3: The effects NLO and UVA crosslinking.

5.6 References

Akhtar, S., Bron, A. J., Salvi, S. M., Hawksworth, N. R., Tuft, S. J., & Meek, K. M. (2008). Ultrastructural analysis of collagen fibrils and proteoglycans in keratoconus. Acta ophthalmologica, 86(7), 764-772.

Bron AJ (1988): Keratoconus. Cornea 7:
163–169.
Bron AJ & Rabinowitz YS (1996): Corneal dystrophies and keratoconus. Curr Opin Ophthalmol 7: 71–82.

Chai, D., Gaster, R. N., Roizenblatt, R., Juhasz, T., Brown, D. J., & Jester, J. V. (2011). Quantitative assessment of UVA-riboflavin corneal cross-linking using nonlinear optical microscopy. Investigative ophthalmology & visual science, 52(7), 4231-4238.

Kamaev, P., Friedman, M. D., Sherr, E., & Muller, D. (2012). Photochemical kinetics of corneal cross-linking with riboflavin. Investigative ophthalmology & visual science, 53(4), 2360-2367.

Knox, C. N., Tyrer, J. R., & Marshall, J. (2012). In vitro quantification of the stiffening effect of corneal cross-linking in the human cornea using radial shearing speckle pattern interferometry. Journal of refractive surgery (Thorofare, NJ: 1995), 28(7), 503-508.

Kohlhaas, M., Spoerl, E., Schilde, T., Unger, G., Wittig, C., & Pillunat, L. E. (2006). Biomechanical evidence of the distribution of cross-links in corneastreated with riboflavin and ultraviolet A light. Journal of Cataract & Refractive Surgery, 32(2), 279-283., M., Spoerl, E., Schilde, T., Unger, G., Wittig, C., & Pillunat, L. E. (2006). Biomechanical evidence of the distribution of cross-links in corneastreated with riboflavin and ultraviolet A light. Journal Cataract & Refractive Surgery, 32(2), 279-283.

Meek, K. M., Tuft, S. J., Huang, Y., Gill, P. S., Hayes, S., Newton, R. H., & Bron, A. J. (2005). Changes in collagen orientation and distribution in keratoconus corneas. Investigative ophthalmology & visual science, 46(6), 1948-1956.

Rabinowitz YS, Rasheed K, Yang H & Elashoff J (1998): Accuracy of ultrasonic pachymetry and videokeratography in detecting keratoconus. J Cataract Refract Surg 24: 196–201.

Seifert, J., Hammer, C. M., Rheinlaender, J., Sel, S., Scholz, M., Paulsen, F., & Schäffer, T. E. (2014). Distribution of Young's modulus in porcine corneas after riboflavin/UVA-induced collagen cross-linking as measured by atomic force microscopy. PloS one, 9(1), e88186.

Sherwin T, Brookes NH, Loh IP, Poole CA & Clover GM (2002): Cellular incursion into Bowman's membrane in the peripheral cone of the keratoconic cornea. Exp Eye Res 74: 473–482.

Spoerl, E., Huhle, M., & Seiler, T. (1998). Induction of cross-links in corneal tissue. Experimental eye research, 66(1), 97-103.

Takahashi, A., Nakayasu, K., Okisaka, S., & Kanai, A. (1990). [Quantitative analysis of collagen fiber in keratoconus]. Nippon Ganka Gakkai Zasshi, 94(11), 1068-1073.

Wollensak, G., Hammer, C. M., Spörl, E., Klenke, J., Skerl, K., Zhang, Y., & Sel, S. (2014). Biomechanical efficacy of collagen crosslinking in porcine cornea using a femtosecond laser pocket. Cornea, 33(3), 300-305.

Wollensak, G., Spoerl, E., & Seiler, T. (2003). Riboflavin/ultraviolet-A–induced collagen crosslinking for the treatment of keratoconus. American journal of ophthalmology, 135(5), 620-627.

Wollensak, G., Spoerl, E., & Seiler, T. (2003). Stress-strain measurements of human and porcine corneas after riboflavin–ultraviolet-A-induced cross-linking. Journal of Cataract & Refractive Surgery, 29(9), 1780-1785.

CHAPTER 6

Conclusions and Future Work

6.1 Conclusions

The primary goal of this work was to build an ARFEM device capable of measuring corneal elastic properties. To this end, the work has been a success. Based on the complex, inhomogeneous structural properties of the cornea, as outlined in Chapter 1, it was necessary that the device have high spacial resolution. This was accomplished by introducing an acoustic contrast agent in the form of a femtosecond laser created microbubble. Without the microbubble, axial measurements without the need to section the cornea would have been virtually impossible. The hypothesis was that application of acoustic radiation force to a femtosecond laser generated bubble and subsequent imaging of the bubble displacement would allow spatially resolved measurement of corneal elastic properties.

The results of the ARFEM study in gelatin phantoms and the pilot measurement in a porcine cornea demonstrated the potential of ARFEM for measuring human corneal elastic properties. ARFEM provided reliable results in gelatin phantoms which were comparable to established methods. The micro-indentation technique served as a perfect comparison due to the similar amounts of strain induced by the measurements (a few microns). Bubble displacement was inversely proportional to local elasticity, while the displacement paths were predictable and adhered to the Voigt model for viscoelastic tissue. The measured elasticity of the gelatin phantoms scaled linearly with increasing concentration while bubble displacements scaled linearly with linearly increasing acoustic intensity.

Unpredictable acoustic interference in the form of standing waves were effectively removed by increasing the working distance of the laser objective and frequency sweeping the

force pulse, thus greatly improving the reliability of the ARFEM device. Before this was accomplished, bubbles regularly traveled backwards towards the transducer itself, confounding measurements. The elimination of the noise in the bubble tracking signal caused by high intensity bleed from the push pulse has un-masked the full path of the bubble in response to an acoustic radiation force. The notched force pulse completely insulated the pulse echo imaging from the high intensity disturbance of the force pulse. With these improvements, ARFEM demonstrated significant potential to provide highly localized elasticity measurements in the human cornea.

This study found that there is a unique distribution of elasticity both axially and radially throughout the cornea. The anterior cornea was found to be consistently stiffer than the posterior in the central and mid cornea, with the trend reversing near the periphery. While ARFEM results in the central cornea are in reasonable agreement with other techniques including needle indentation and torsional rheometry, lack of mechanical data in the peripheral cornea make comparisons difficult. It is however clear that the full picture of corneal biomechanics is quite broad, involving complex and inhomogenous collagen microstructure to varying concentration of proteoglycans throughout the cornea. A better understanding of these variables along with elasticity measurements, especially in the peripheral cornea, would certainly help in completing the picture.

It was demonstrated that ARFEM is an effective technique for validating the efficacy of crosslinking procedures. It was shown that both NLO CXL and UVA CXL succeed in strengthening the cornea, in good agreement with other techniques. NLO CXL is a promising new technique that has the potential for highly customized and tuneable selective stiffening of

the cornea. Due to its multiphoton action only in the focal volume, NLO CLX has a distinct advantage of traditional UVA CXL.

6.2 Future Work

6.2.1 Anisotropy in the Cornea

It is well understood that the cornea is an anisotropic tissue. The cornea is comprised of hundreds of lamellae running limbus to limbus, with many interjecting in the Bowman's membrane and back into the stroma. Measurements parallel to the direction of the lamellae instead of perpendicular to them would surely provide fascinating new data. Figure 6.1 illustrates a likely setup capable of achieving this goal. At a given location in the cornea, a bubble would be created and its displacement first measured at a negative angle. Next, the transducer would be shifted and the bubble would be displaced and measured from the positive angle. The displacement vectors could be broken down into orthogonal components, parallel and perpendicular the corneal surface, thus revealing normal and transverse elasticity.

6.2.2 Whole Globe Experiments

A limitation of the current procedure is the necessity of removing the cornea from the globe and embedding it in gelatin. The ability to measure the biomechanical properties of a cornea pressurized at IOP while intact with the globe would be a significant leap forward in this research. Not only would it allow for measurements to be conducted closer to physiological conditions, but hydration could be precisely controlled. To this end, the laser and ultrasound would ideally be confocal and coming from the same direction.

6.3 Closing Remarks

Bubble based acoustic radiation force elastic microscopy is a powerful elastography tool with superb resolution, especially when considering ocular media. This technique has potential to further help us understand the mechanics of the cornea and if given enough attention the potential to serve as a powerful diagnostic tool.
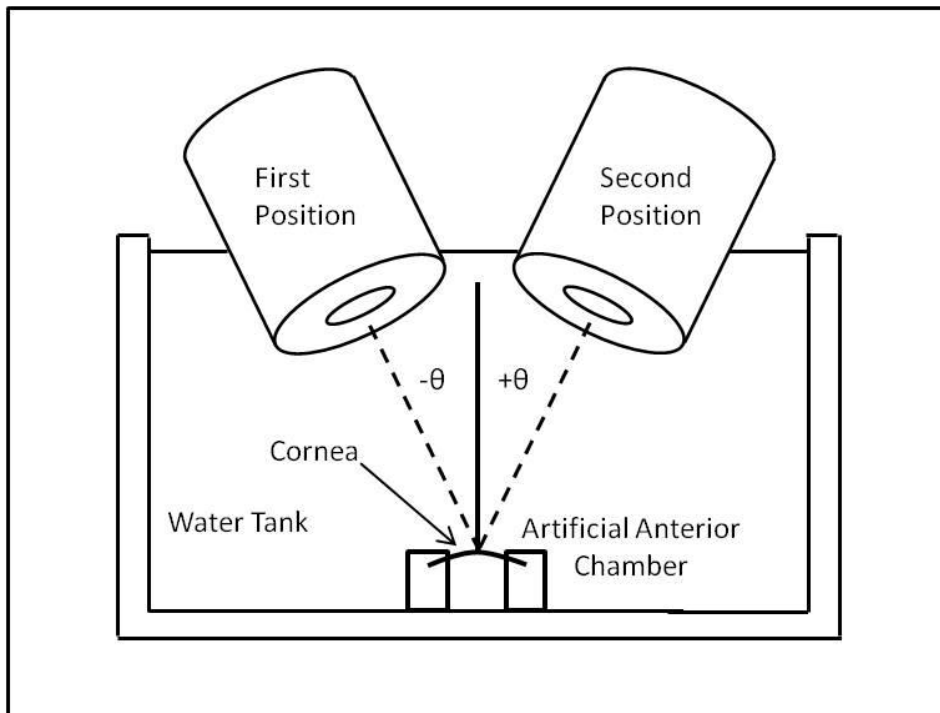
Figure 6.1: Experimental setup for dual angle ARFEM. A single confocal transducer is moved between two angular positions. Transverse elastic components can be calculated.